DOI:
10.1161/CIRCGENETICS.116.001431

Document Version
Publisher's PDF, also known as Version of record

Original Article

OPEN

Combination of Whole Genome Sequencing, Linkage, and Functional Studies Implicates a Missense Mutation in Titin as a Cause of Autosomal Dominant Cardiomyopathy With Features of Left Ventricular Noncompaction

Robert Hastings, MBChB, DPhil, MRCP*; Carin P. de Villiers, PhD*; Charlotte Hooper, PhD; Liz Ormondroyd, PhD, MSc; Alistair Pagnamenta, PhD; Stefano Lise, PhD; Silvia Salatino, PhD; Samantha J.L. Knight, PhD, CBiol, MSB, FRCPath; Jenny C. Taylor, PhD; Kate L. Thomson, BSc, FRCPath; Linda Arnold, MSc; Spyros D. Chatziefthimiou, PhD; Petr V. Konarev, PhD; Matthias Wilmanns, PhD; Elisabeth Ehler, PhD; Andrea Ghisleni, MSc; Mathias Gautel, MD, PhD; Edward Blair, BMSc, MBChB; Hugh Watkins, MD, PhD, FRCP; Katja Gehmlich, PhD

Background—High throughput next-generation sequencing techniques have made whole genome sequencing accessible in clinical practice; however, the abundance of variation in the human genomes makes the identification of a disease-causing mutation on a background of benign rare variants challenging.

Methods and Results—Here we combine whole genome sequencing with linkage analysis in a 3-generation family affected by cardiomyopathy with features of autosomal dominant left ventricular noncompaction cardiomyopathy. A missense mutation in the giant protein titin is the only plausible disease-causing variant that segregates with disease among the 7 surviving affected individuals, with interrogation of the entire genome excluding other potential causes. This A178D missense mutation, affecting a conserved residue in the second immunoglobulin-like domain of titin, was introduced in a bacterially expressed recombinant protein fragment and biophysically characterized in comparison to its wild-type counterpart. Multiple experiments, including size exclusion chromatography, small-angle x ray scattering, and circular dichroism spectroscopy suggest partial unfolding and domain destabilization in the presence of the mutation. Moreover, binding experiments in mammalian cells show that the mutation markedly impairs binding to the titin ligand telethonin.

Conclusions—Here we present genetic and functional evidence implicating the novel A178D missense mutation in titin as the cause of a highly penetrant familial cardiomyopathy with features of left ventricular noncompaction. This expands the spectrum of titin's roles in cardiomyopathies. It furthermore highlights that rare titin missense variants, currently often ignored or left uninterpreted, should be considered to be relevant for cardiomyopathies and can be identified by the approach presented here. **(*Circ Cardiovasc Genet*. 2016;9:426-435. DOI: 10.1161/CIRCGENETICS.116.001431.)**

Key Words: cardiomyopathy ■ left ventricular noncompaction ■ missense mutation ■ telethonin ■ titin ■ whole genome sequencing

Cardiomyopathies are a diverse group of diseases affecting the heart muscle[1]; many of them are inherited and transmitted in autosomal dominant patterns. The first cardiomyopathy genes were identified by genome-wide linkage analysis in large families.[2] In practice, however, the small size of most families, or even the availability of members of larger families, often limits the power of linkage analysis. Recently, high throughput next-generation sequencing techniques have become widely accessible, making whole genome sequencing (WGS) cost-effective and time-effective. However, the abundance of variation in the human genome[3] makes it difficult to distinguish rare benign variants from rare disease-causing mutations in an isolated individual, even with growing knowledge of variants in population cohorts (eg, >60 000 sequenced exomes in the Exome Aggregation Consortium (ExAC) database, http://exac.broadinstitute.org/). Next-generation sequencing poses, therefore, a significant clinical challenge: the capability to assess variants

Editorial, see p 392
Clinical Perspective on p 435

Received March 10, 2016; accepted August 31, 2016.

*Drs Hastings and de Villiers contributed equally to this work.

The Data Supplement is available at http://circgenetics.ahajournals.org/lookup/suppl/doi:10.1161/CIRCGENETICS.116.001431/-/DC1.

Correspondence to Katja Gehmlich, PhD, Division of Cardiovascular Medicine, Radcliffe Department of Medicine, University of Oxford, Level 6, West Wing John Radcliffe Hospital, Headley Way, Oxford OX3 9DU, United Kingdom. E-mail katja.gehmlich@cardiov.ox.ac.uk

as pathogenic lags significantly behind variant identification, especially for nonsynonymous point mutations.[4,5] Algorithmic predictors are currently unable to accurately assess their exact impact on protein–protein interactions or even on protein folding. Experimental validation of genetic variants is, therefore, an increasingly indispensable component of next-generation sequencing discoveries.

In the current study, we combine WGS with linkage analysis in a medium-sized family affected by cardiomyopathy, with features of left ventricular noncompaction cardiomyopathy (LVNC). By performing WGS in 2 family members, filtering against variants seen in normal population cohorts and using linkage information derived from single nucleotide polymorphism (SNP) arrays of 13 family members, we could identify a missense variant in the titin gene (*TTN*) as the most plausible cause of disease in the family. Functional data generated from biophysical and protein-binding experiments on this titin missense variant provide further support of a causative role in cardiomyopathy through domain misfolding and destabilization, resulting in impaired binding to the ligand telethonin (also known as t-cap).

Methods

Clinical Evaluation

The study was approved by the Oxfordshire Research Ethics Committee B (REC Ref 09/H0605/3), and all subjects gave informed consent. A 3-generational family with history of cardiomyopathy was recruited. Clinical assessment and genetic studies were performed in available family members, who had clinical examination, ECG, echocardiography (with contrast agent where appropriate), and cardiac magnetic resonance imaging, if possible. Diagnosis of cardiomyopathy was based on established criteria. The diagnosis of LVNC was based on published criteria from echocardiographic or cardiac magnetic resonance imaging[6,7]: the compaction ratio, that is, the ratio of the thickness of noncompacted to compacted myocardium >2.3 measured on magnetic resonance imaging in diastole or >2.0 on echocardiography in systole, was used to diagnose LVNC.

Genetic Studies

SNP array genotyping was performed using the Illumina HumanCytoSNP-12v1 BeadChip (Illumina, San Diego, CA), containing nearly 300 000 genetic markers, according to the manufacturer's protocols. A refined subset of roughly 24 000 SNPs in approximate linkage equilibrium was generated using the software PLINK v1.07[8] and the HapMap genotype file available from the PLINK website (http://pngu.mgh.harvard.edu/purcell/plink/). Linkage analysis of the SNP subset was performed using MERLIN v1.1.2,[9] specifying an autosomal dominant disease model. Genomic intervals with logarithm of the odds scores >0, compatible with segregation of variants in these regions, were selected for downstream analyses.

WGS was performed on genomic DNA extracted from peripheral blood as part of the WGS500 project as described previously.[10]

Sequence reads from the affected individuals were mapped to the human reference genome (hs37d5 version of build 37) using STAMPY.[11] Duplicate reads were removed with PICARD (http://broadinstitute.github.io/picard/). The software Platypus (version 0.8.1, default parameters)[12] was used jointly on the two.bam files to call SNPs and short (<50 bp) indels across both samples.

All the 5 946 161 identified variants were annotated with an in-house pipeline based on the Variant Effect Predictor Ensembl framework (version 77).[13] Several additional databases were used to integrate the information provided by Variant Effect Predictor (Table I in the Data Supplement). Known associations with diseases were screened using HGMD (http://www.hgmd.cf.ac.uk/ac/index.php) and ClinVar.[14]

Variants were filtered by in-house Python scripts based on criteria outlined in Table I in the Data Supplement (steps 1–10), followed by manual inspection (steps 11–13). The variants remaining after step 10 are documented in Results and in Tables II and III in the Data Supplement. Confirmatory Sanger sequencing was performed with the primers listed in Table IV in the Data Supplement.

Both SNP and WGS data were interrogated also for clinically relevant copy number variants using Nexus Copy Number 7.5.2 Discovery Edition (BioDiscovery, Hawthorne, CA; see Methods in the Data Supplement).

Functional Characterization of the Titin Missense Variant

The mutation was introduced into human titin Z1Z2 constructs (amino acids 1–196, accession no ACN81321.1) for bacterial and mammalian expression using Quikchange II XL (Agilent) with primers given in Table IV in the Data Supplement. Bacterial expression and purification was performed as previously described.[15] Size exclusion chromatography–Tridetector analysis (light scattering, refractive index, and UV absorbance), small-angle x ray scattering experiments, circular dichroism spectroscopy, and thermolysin digests were essentially performed as described,[15–18] and experimental details are given in the Data Supplement.

Neonatal rat cardiomyocyte (NRC) cultures were established and transfected[16] using hemagglutinin-tagged expression constructs and counterstained for titin T12 epitope[19] or telethonin (mouse monoclonal antibody, Santa Cruz) 48 hours post transfection and analyzed by confocal microscopy.

Glutathione S-transferase (GST) pulldown assays were performed as described[20] using mammalian expression constructs for telethonin amino acids 1 to 90 and 1 to 167 fused to GST and titin Z1Z2 fused to GFP (pEGFP-N1, Clontech) in transfected COS-1 cells. Förster Resonance Energy Transfer experiments from transfected COS-1 cells and the assessment of reduced protein stability in NRC and COS-1 cells are described in the Data Supplement.

Results

The proband was a 20-year-old male (II-3 in Figure 1A) who died suddenly in hospital in 1970 having presented with rapidly decompensating congestive heart failure; at postmortem, his heart (680 g) had evidence of dilatation and both macroscopic and microscopic hypertrophy but no myocyte disarray. His brother (II-4) was later found to have an enlarged heart with wall thickness at the upper limit of normal and marked hypertrabeculation. The proband's sister (II-2) presented with a non–ST-segment–elevation myocardial infarct because of coronary embolus at the age of 61 years. LVNC with mild left ventricular dilatation and apical hypertrophy was diagnosed at this time (Figure 1B and 1C). Cascade screening identified the same condition in further family members with consistent clinical features of adult onset cardiomyopathy with features of LVNC. Five affected family members had sufficient noncompaction to meet the diagnostic criteria for LVNC, while 3 others with early or mild disease had lesser extent of hypertrabeculation but clear evidence of cardiomyopathy with left ventricular dilatation or systolic dysfunction (Figure 1A and Table 1; Figure I in the Data Supplement). Aside from the proband who had advanced congestive failure, there were no arrhythmic features in any affected family member, nor were there any extracardiac (eg, neuromuscular) manifestations.

Identification of TTN Mutation A178D Segregating With Disease

Affected first cousins III-1 and III-4 were selected for WGS. Sequencing was performed by Illumina Cambridge as 100-bp paired-end reads to a mean coverage of 56.9× and 52.0×,

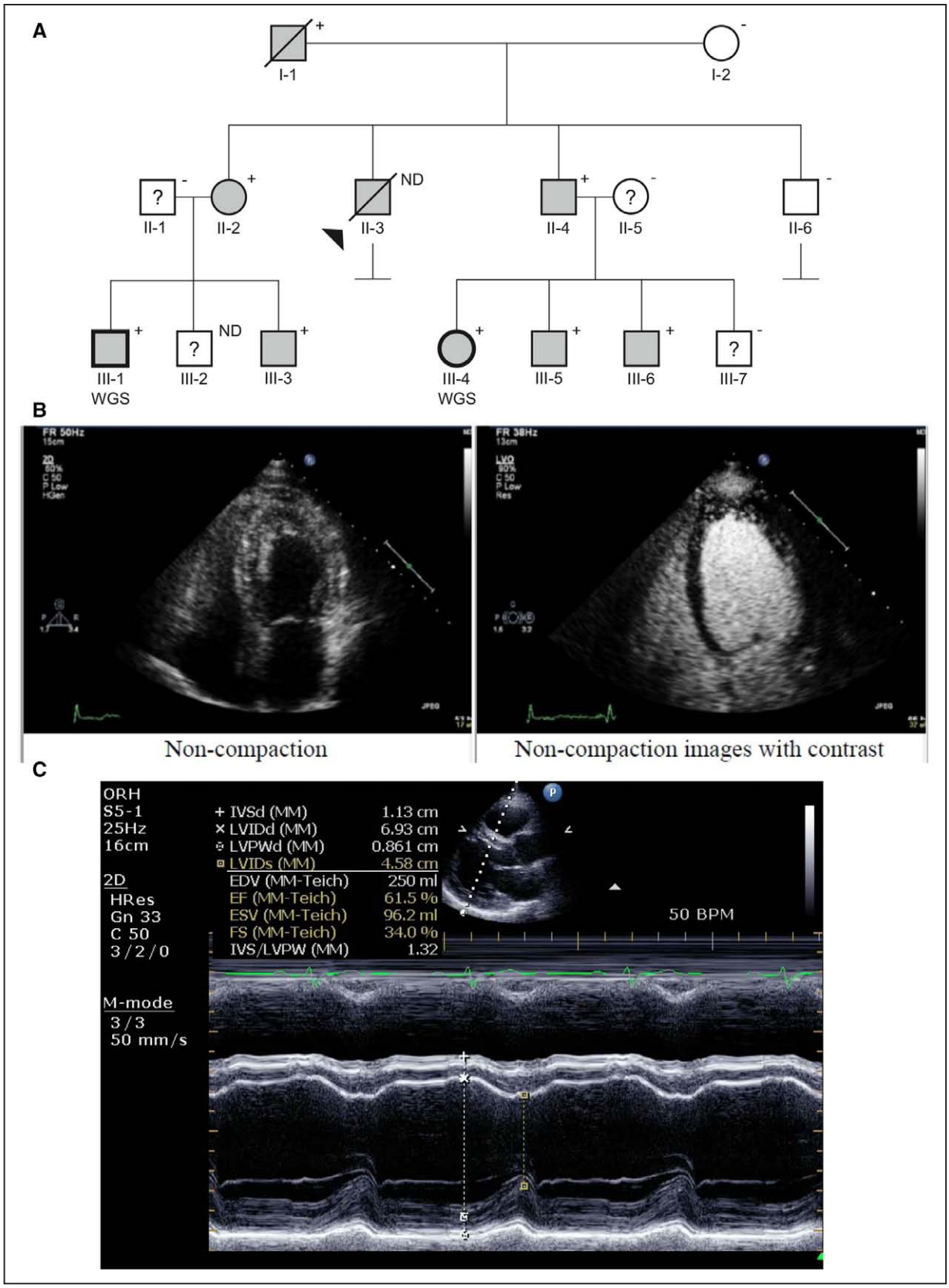

Figure 1. **A**, Pedigree of the family; males depicted as squares; females, circles; slanted symbols, deceased individuals. Clinically affected individuals are marked in gray, unaffected are shown in white, and ? means unclassified clinical status. The presence of the *TTN* p.A178D mutation is indicated (+ indicates present; –, absent; ND, not determined.) Individuals selected for whole genome sequencing (WGS) are marked with thicker symbols (III-1 and III-4). **B**, Echocardiogram images showing the characteristic spongy appearance of non-compaction in individual II-2 with and without contrast. **C**, Echocardiogram image from individual II-4 showing significant dilatation, but maintaining a thickened myocardium and preserved ejection fraction.

respectively, such that 99% of the genome was covered at 20× or more in both samples, identifying 5 946 161 variants shared by the 2 individuals. In addition, SNP arrays were performed on all individuals of the family (except II-3 and III-2; Figure 1A). Neither the SNP array nor WGS data revealed likely causative copy number variants.

Genomic regions identical by descent were identified through linkage analysis (see Methods and Figure II in the Data Supplement), and out of the 100 789 candidate variants within the 3 linkage regions (on chromosomes 2, 9, and 16), potentially pathogenic ones were selected based on an autosomal dominant model,

Table 1. Summary of Clinical Findings

Symbol	Sex	Age*	Clinical Status†	Genetic Status	Trabeculation Compaction Ratio (CR)‡	IVSD	PWD	LVEDD	LVESD	EF	ECG	Comments
I-1	M	87	Affected	TTN A178D	2.5 (echo)	24	13	40	35	42	Left axis deviation, anteroseptal Q wave	Marked ASH with low EF, CVA, hypertension; meets diagnostic criteria for LVNC (echo)
I-2	F	72	Unaffected	WT	1.8 (echo)	12	11	48	30	76	AF, paced	LVNC excluded (echo), structurally normal heart at age 70 y, moderate concentric LVH by age 85 y
II-2	F	61	Affected	TTN A178D	2.0 (echo)	9	10	53	36	47	Left axis deviation	Mildly thickened apical segments, cardiac embolus at 61 y; meets diagnostic criteria for LVNC (echo)
II-3	M	20	Assumed affected	No DNA								Rapidly progressive HF with sudden death at 20 y (1970); hypertrophy and dilatation at postmortem
II-4	M	37	Affected	TTN A178D	<2 (MRI)	12	12	64	44	57	Normal	Dilated LV, late Gd on MRI, hypertension
II-6	M	42	Unaffected	WT		11	9	50	30	78	Normal	
III-1	M	27	Affected	TTN A178D	2.5 (echo)	12	11	64	42	63	QRS 120 ms	Mild regional systolic dysfunction; meets diagnostic criteria for LVNC (echo)
III-2	M	21	Unclassified	No DNA	0.8 (echo)	13	13	54	37	68	Normal	Mild concentric LVH
III-3	M	32	Affected	TTN A178D	2.8 (MRI)	11	13	52	35	68	Normal	Hypertension; meets diagnostic criteria for LVNC (MRI)
III-4	F	23	Affected	TTN A178D	2.6 (MRI)	8	9	46	32	58	Normal	Meets diagnostic criteria for LVNC (MRI)
III-5	M	25	Affected	TTN A178D	2.0–2.5 (MRI)	10	10	46	27	51	Inferior T-wave inversion	Hypokinesia apical LV incl. septum; borderline for diagnostic criteria for LVNC (MRI)
III-6	M	23	Affected	TTN A178D	1.5 (MRI)	8	9	53	34	48	Q wave and T-wave inversion in lead III	Mild DCM, faint late Gd, borderline dilated LV with mildly impaired function, inferior hypokinesia
III-7	M	21	Unclassified	WT	1.6 (MRI)	9	7	55	38	59	Normal	Documented myocarditis at 21 y (MRI)

Cardiac dimensions are given in mm. Blank cells indicate no data available. AF indicates atrial fibrillation; ASH, asymmetrical septal hypertrophy; CVA, cerebrovascular accident; DCM, dilated cardiomyopathy; EF, ejection fraction (in %); Gd, gadolinium; HF, heart failure; IVSD, interventricular septal thickness at diastole; LVEDD, left ventricular end-diastolic diameter; LVESD, left ventricular end-systolic diameter; LVH, left ventricular hypertrophy; LVNC, left ventricular noncompaction cardiomyopathy; MRI, magnetic resonance imaging; PWD, posterior wall thickness at diastole; and TTN, titin.

*Age of diagnosis or first clinical assessment; however, parameters of most recent cardiac assessment are given (with exception of I-2, where data at first assessment aged 70 y are given, and II-7, where the last assessment before myocarditis is shown).

†Clinical status affected means affected by cardiomyopathy. Whether individuals meet diagnostic criteria for LVNC is shown in the Comments column (whether MRI or echo criteria have been used is shown in brackets).

‡For the definition of trabeculation compaction ratio (CR), see Methods section; the mode of imaging is indicated in brackets. Representative MRI images are shown in Figure I in the Data Supplement.

caused by a rare heterozygous mutation. Variants were filtered accordingly by in-house Python scripts, and the remaining 6 variants were manually inspected (Table II in the Data Supplement). Four of them were excluded: one is assumed to be an artifact because of an incorrect transcript being present in Ensembl and another variant did not segregate with disease in the family; 2 splice variants were predicted to be silent (at positions -5 and -3 of a 3′ splice junction, respectively; for details, see Table III in the Data Supplement). Only 2 final candidate variants were considered conceivably linked to the phenotype: missense changes in *PDP2* and *TTN*, respectively (Table II in the Data Supplement). *PDP2* codes for pyruvate dehyrogenase phosphatase catalytic subunit 2 and has low expression levels in the heart. Although the change E316K is predicted to be damaging by Polyphen and SIFT algorithms (Table II in the Data Supplement), a heterozygous loss-of-function in this enzyme would not be expected to produce a phenotype, and indeed, heterozygous loss-of-function mutations in *PDP1* are clinically silent.[21] The variant is not plausible as a cause of a penetrant-dominant disorder because it is found 6× in 121412 alleles in the ExAC database. Six instances would equal at least 10% of all expected LVNC cases in ExAC, assuming a maximal prevalence of 1:1000 for the disease.[22] This seems to be an implausibly high percentage for a novel, unpublished disease-causing variant. In support, in the 2 largest clinical cardiomyopathy cohorts published to date, the most common reported pathogenic variant (*MYBPC3*, p.Arg502Trp) detected in 104 out of 6179 hypertrophic cardiomyopathy cases (1.7%, 95% confidence interval 1.4%–2.0%) was only observed 3× in ExAC (3/120674), with all other pathogenic variants for hypertrophic cardiomyopathy or dilated cardiomyopathy (DCM) being present 0 or 1 time only.[23]

The second variant is found in *TTN*, the gene that codes for titin, an abundant skeletal muscle and heart-specific protein with crucial functions[24,25] (and reviewed in Gerull[26] et al). Mutations in titin have been associated with cardiomyopathy and skeletal myopathy (reviewed in Chauveau et al[27]). The identified missense variant c.533C>A in *TTN*, which codes for a p.A178D change at the amino acid level, is absent in ExAC. Sanger sequencing confirmed the cosegregation of the heterozygous mutation with disease in all affected individuals of the family (Figure 1; Figure IIIA in the Data Supplement; logarithm of the odds score 2.1). Thus, comprehensive whole genome analysis reveals this as the most plausible causative mutation in the family.

Functional Studies

Prediction of Deleterious Effects of the Mutation

Each single molecule of the giant protein titin spans half a sarcomere from the Z disk to the M band.[28] The first 2 immunoglobulin-like domains (Z1Z2) of titin are located in the Z disk and form a superstable complex with telethonin.[29] The A178 position is evolutionarily well conserved back to zebrafish and lamprey. Additionally, A178 is located in a highly conserved structural section (Figure IIIB in the Data Supplement), the β-strand F of the second immunoglobulin domain of Z1Z2, neighboring the β-strand G of titin Z2, which forms a strong and extended interaction with the β-strands of telethonin[30] (Figure 2A). The A178D mutation is predicted to directly affect the β-strands B and C and the loop connecting the β-strands B and C because of steric hindrance of D178 with V127 and P133, respectively (Figure 2B). Thus, the insertion of a charged residue in this position is likely to have significant impact on the secondary structure of this domain and could potentially cause misfolding of the protein.

Altered Protein Characteristics of Purified Titin Z1Z2 A178D Recombinant Fragment

To assess how the A178D mutation affects the folding and stability of the protein, recombinant titin Z1Z2 WT and A178D were

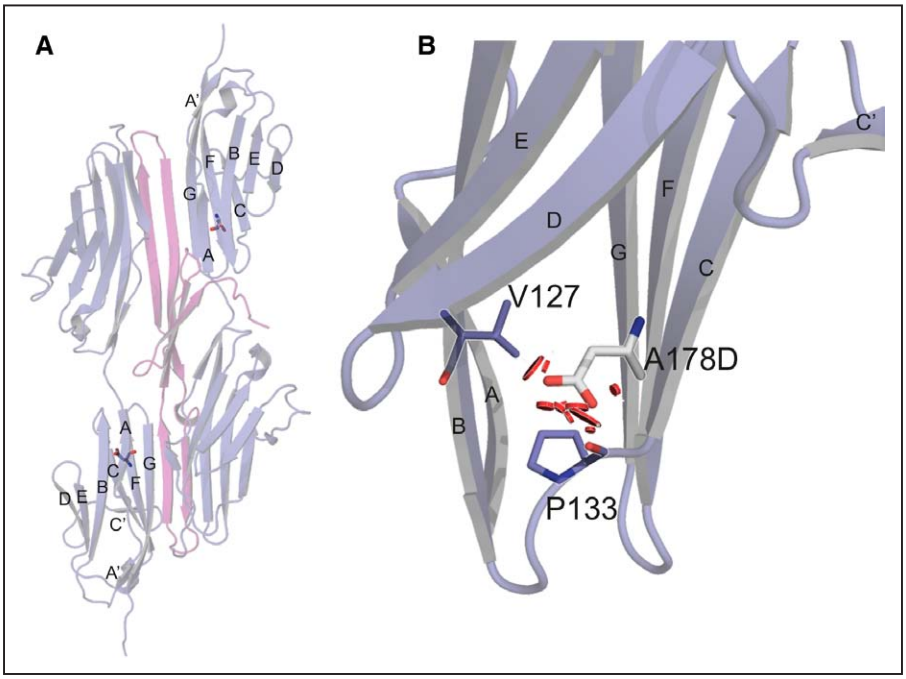

Figure 2. **A**, Position of the *TTN* p. A178D on a structural model (pdb: 1YA5) of the titin Z1Z2 domains (purple) in complex with telethonin (pink). **B**, Close-up of the site of mutation. The red discs show van der Waals overlaps or steric clashing that A178D is predicted to cause with valine127 and proline133. The figures of the crystal structure were generated by Pymol (http://www.pymol.org).

expressed in *Escherichia coli* and purified under native conditions. Of note, the yield of the soluble protein fraction was consistently lower for A178D compared with WT preparations, despite equal total expression levels (data not shown). Circular dichroism spectroscopy demonstrated a typical β-sheet signature for WT Z1Z2 (Figure 3A). In contrast, the spectrum for Z1Z2 A178D differs significantly: although the characteristic negative band at 216 nm is still present, but slightly shifted, there was no significant positive band at around 200 nm. The absence of this band, associated with β-sheet conformation, and the presence of a negative peak at around 198 nm, characteristic of random coil structures, indicate that the Z1Z2 A178D mutant is partially unfolded.

In support, thermal denaturation experiments for Z1Z2 A178D showed high fluorescence signal already at low temperatures, suggesting solvent exposed hydrophobic residues because of partial unfolding. No melting temperature can be deducted for titin Z1Z2 A178D, in contrast to the WT protein, which has a melting temperature of 62°C, typical for immunoglobulin domains (Figure IV in the Data Supplement). Small-angle x ray scattering experiments confirmed the presence of unfolded parts/flexible domains in Z1Z2 A178D, as shown by the Kratky plot (Figure VA in the Data Supplement), whereas Z1Z2 WT displays a typical profile for folded structures.

The domain destabilization as a consequence of partial unfolding is evidenced by the formation of higher oligomers (≈20-mers) for the Z1Z2 A178D mutant in vitro. Size exclusion chromatography and Tridetector analysis revealed that in contrast to the monomeric Z1Z2 WT, the A178D mutant eluted in 2 peaks, corresponding predominantly to higher molecular aggregates and to a lesser extent to dimeric protein (Figure 3B and Table 2). Small-angle x ray scattering measurements also confirmed that Z1Z2 WT is monomeric, whereas Z1Z2 A178D is found in a higher oligomeric state (Table 2; Figure VB in the Data Supplement).

In conclusion, the mutation A178D leads to partial misfolding of bacterially expressed Z1Z2 protein fragment.

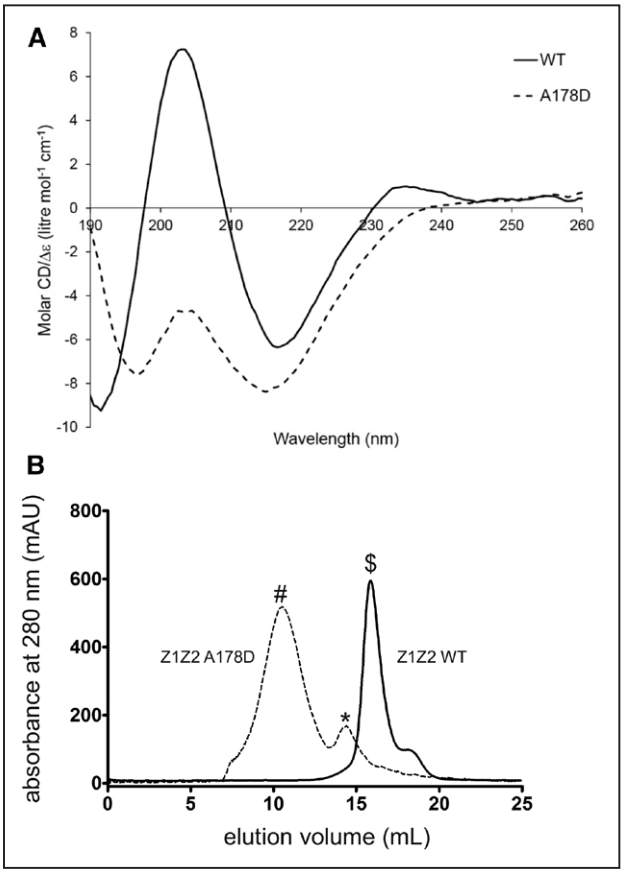

Figure 3. **A**, Circular dichroism (CD) spectroscopy of purified titin Z1Z2 fragments (WT solid line and A178D dashed line). **B**, Size exclusion chromatography for titin Z1Z2 fragments (WT solid line and A178D dashed line). Z1Z2 WT elutes as monomeric protein ($), whereas peaks corresponding to dimer (*) and higher molecular aggregates (#) are observed for Z1Z2 A178D.

Reduced Stability of Titin Z1Z2 A178D as a Consequence of the Partial Misfolding

When performing denaturing gel electrophoresis, a degradation product was observed exclusively for Z1Z2 A178D preparations (arrowhead in Figure 4A), and on thermolysin treatment, only Z1Z2 A178D showed rapid degradation, whereas Z1Z2 WT was resistant to the protease treatment (Figure 4B). In addition, Z1Z2 A178D showed reduced stability when expressed in neonatal rat cardiomyocytes and COS-1 cells (Figure 4C; Figure VI in the Data Supplement), suggesting that the mutation destabilizes Z1Z2 also in a physiological, cellular environment. However, formation of large aggregates was not observed in transfected cells expressing Z1Z2 A178D (Figure 4D; Figure VII in the Data Supplement).

Impaired Binding to Telethonin

Localization of transfected Z1Z2 was not altered in the presence of the A178D mutation (Figure 4D). To assess the consequences of the mutation on binding telethonin, semiquantitative GST pulldown assays were performed with titin Z1Z2 and telethonin coexpressed in mammalian cells. Z1Z2 A178D showed impaired binding to 2 telethonin constructs (Figure 5A and 5B). The interaction between titin and telethonin was further quantified in Förster Resonance Energy Transfer experiments, where close proximity of proteins in a complex allows energy transfer from cyan fluorescent protein to yellow

Table 2. Biophysical Characterization of Recombinant Z1Z2 WT and A178D Protein Fragments

	Titin Z1Z2 WT	*Titin Z1Z2* A178D
Calculated molecular weight, kDa	22.7	22.8
Size exclusion chromatography		
Retention time, mL	15.7	9.9 (1st peak)
		14.4 (2nd peak)
Static light scattering		
Molecular weight, kDa	21±2	452±45 (1st peak)
		45±4 (2nd peak)
Small-angle x ray scattering		
V_p, excluded volume of the hydrated particle, nm^3	40±5	305±20
R_g, radius of gyration, nm	3.10±0.05	6.8±0.1
D_{max}, maximum particle size, nm	10.5±0.5	25.0±1.0
Normalized Kratky plot	Folded	Partly unfolded/ flexible domains

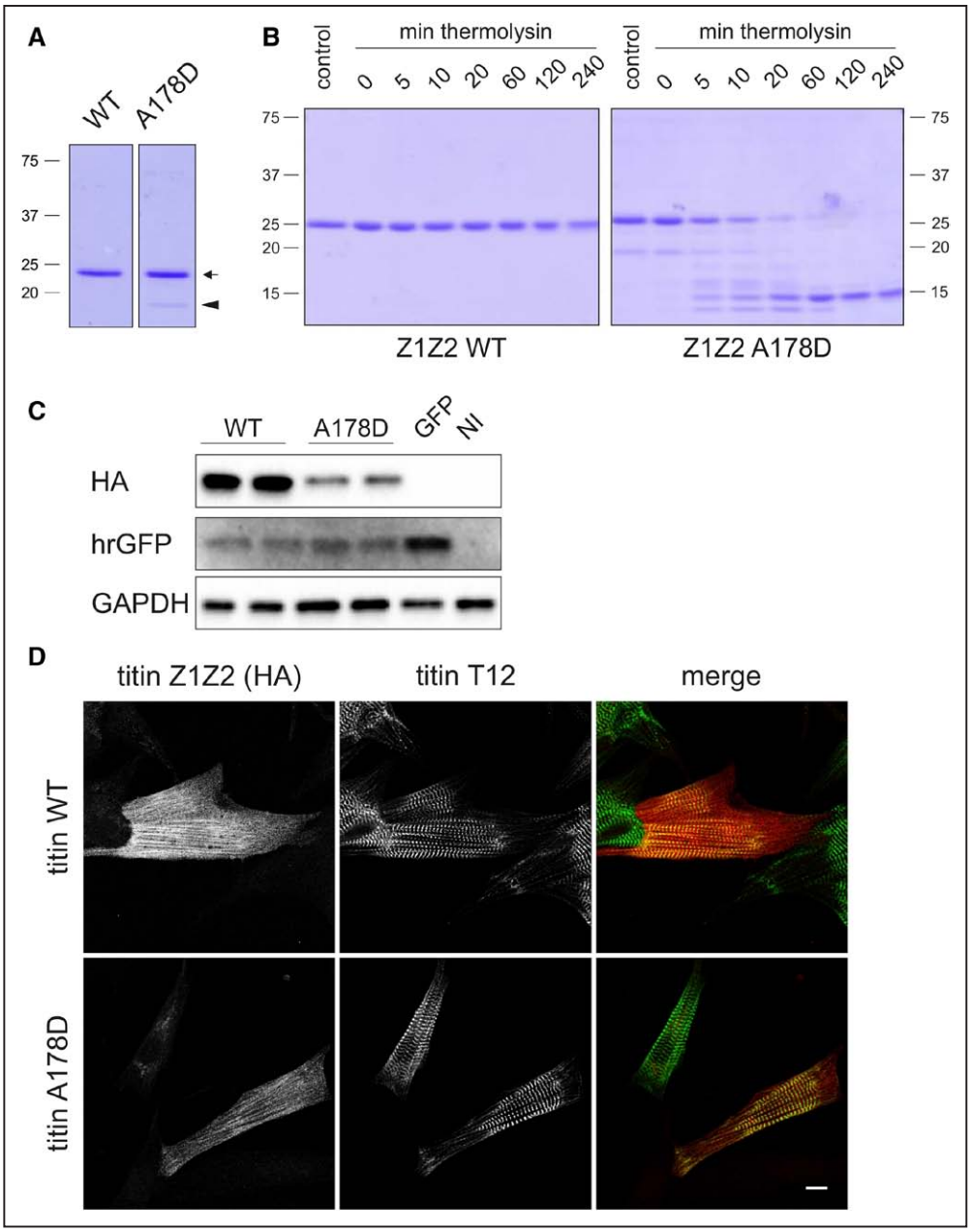

Figure 4. Destabilization of the titin Z1Z2 fragment in the presence of the A178D mutation. **A**, Denaturing gel-electrophoresis of purified titin Z1Z2 fragments (WT and A178D) expressed in *Escherichia coli.* The WT fragment is detected as a single band of 23 kDa (arrow). Only for Z1Z2 A178D, a degradation product (arrowhead) is observed. The position of marker proteins and their size (in kD) is indicated. **B**, Titin Z1Z2 protein fragments (**left**, WT; **right**, A178D) were incubated with protease thermolysin for the length indicated. Control: titin Z1Z2 protein sample without thermolysin. A stable degradation fragment of ≈15 kDa is observed for the mutant titin Z1Z2. The position of marker proteins and their size (in kD) is indicated. **C**, Decreased stability of titin Z1Z2 A178D in neonatal rat cardiomyocytes (NRC). NRC were infected in duplicates with adenoviral particles for hemagglutinin (HA)-tagged titin Z1Z2 (WT or A178D, MOI 5). Infection with parental empty vector (GFP) and noninfected cells (NI) served as controls. Steady-state titin fragment protein amount was assayed by Western blotting for the HA tag. Probing for humanized Renilla reniformis green fluorescent protein (hrGFP) served as infection control, and probing for endogenous GAPDH served as loading control. Despite equal infection rates (for confirmatory control experiments see Figure VIA in the Data Supplement), less titin A178D protein fragment was detected, indicating reduced stability in NRC. **D**, Localization of titin Z1Z2 in NRC. Cells were transfected with constructs coding for HA-tagged titin Z1Z2 WT (top, first row) or titin Z1Z2 A178D (bottom, first row) mutant protein fragment and counterstained for endogenous titin with T12 antibody (middle row, Z-disk proximal epitope, but not recognizing the transfected titin Z1Z2 protein fragment). Merged images are shown in the third row; HA, in red; endogenous titin, in green. Scale bar represents 10 μm.

fluorescent protein between 2 fusion protein constructs.[31] By introducing the A178D mutation into a Z1Zr3-cyan fluorescent protein construct, Förster Resonance Energy Transfer efficiency to telethonin-yellow fluorescent protein was almost abolished (Figure 5C and 5D), validating and quantifying the observation that A178D impairs binding to telethonin in the cellular context.

Taken together, our functional data suggest that the A178D mutant may affect protein folding and stability and impairs binding to telethonin, thus, supporting its pathogenic potential.

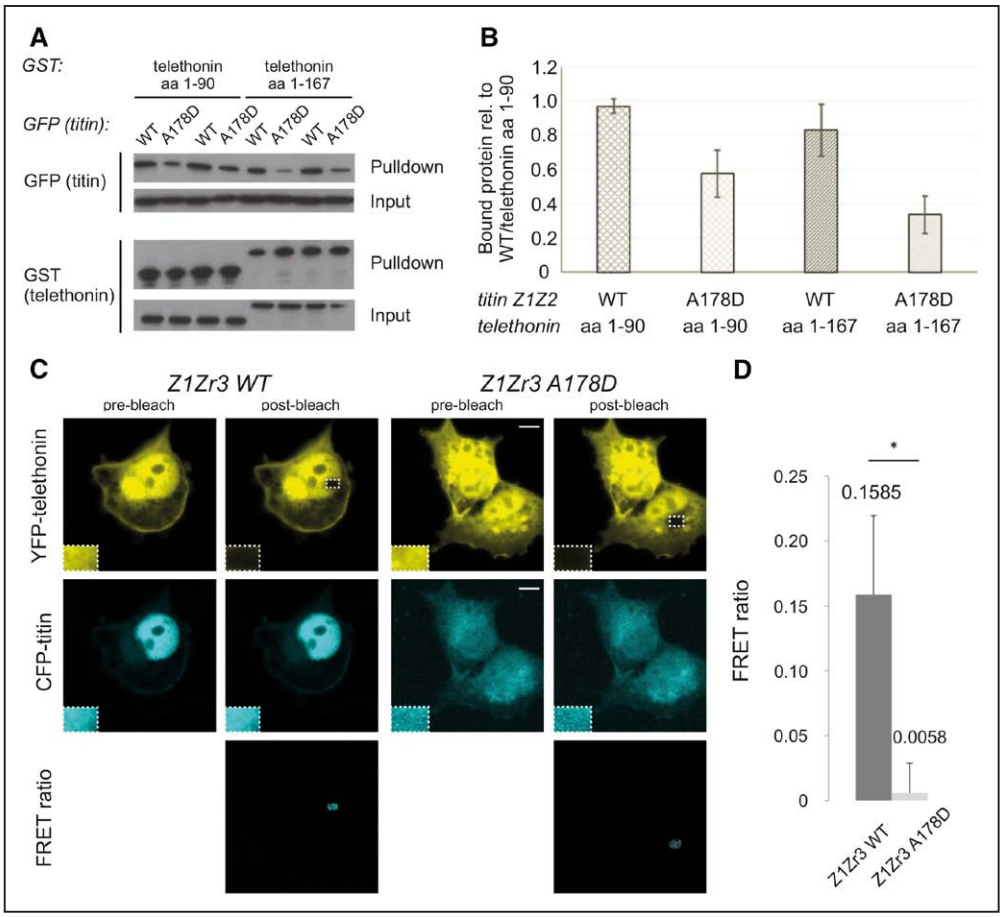

Figure 5. Functional implications of the titin Z1Z2 A178D mutation. **A**, Semiquantitative Glutathione S-transferase (GST) pulldown assays using telethonin fragments fused to GST (left aa 1–90, right full length) and titin Z1Z2 fragments (WT and A178D as indicated) as GFP fusions expressed in COS-1 cells. Bound titin-GFP fragments are detected by Western blotting (top row); input lysate controls are shown in the second row. Pulled down GST-telethonin fragments are shown in row three, as well as lysate controls (bottom row). **B**, Quantification of GST pulldown experiments from panel **A** visualizes reduced binding of titin Z1Z2 to telethonin in the presence of the A178D mutation; values are expressed as bound protein relative to lysate, with the first WT experiment set to 100% (n=2 per group, values expressed as mean with standard deviation for error bars; one representative experiment of 3 independent ones is shown). Because of the semiquantitative nature of the experiments, no statistical test was performed. **C**, Förster Resonance Energy Transfer (FRET) experiments using COS-1 cells cotransfected with telethonin (aa 1–90) fused to yellow fluorescent protein (YFP; first row) and titin Z1Zr3 fused to cyan fluorescent protein (CFP; second row). Images pre and post bleach are shown. FRET ratios are shown in the third row. Insets show magnification of indicated area. Scale bar represents 10 μm. **D**, Quantification of FRET efficiency for titin Z1Zr3 WT/A178D and telethonin pairs. The A178D mutation reduces the FRET efficiency from ≈0.15 to 0.01, indicating a dramatic loss of binding ability (WT n=20 and A178D n=26 cells; *P<0.0001 unpaired Student's t test).

Discussion

In this study, we present a 3-generation family with multiple individuals affected by cardiomyopathy with features of LVNC, systolic impairment, and an autosomal dominant inheritance pattern. Of note, the affected family members show a consistent phenotype with prominent hypertrabeculation as the main abnormality in the majority; this is relatively unusual because it is more typical to see LVNC in individual members of families with other forms of cardiomyopathy.

We used a combination of WGS in 2 affected individuals and linkage analysis in 13 family members; this approach identified only 2 rare candidate variants across the whole genome that segregated with the autosomal dominant cardiomyopathy. Because one of the identified genes (*PDP2*) is barely expressed in the heart, and the variant appears in implausible high numbers in the ExAC database, it is extremely unlikely to be disease causative. In contrast, titin, the gene affected by the other missense variant (*TTN* p.A178D), has crucial functions in the heart and is a known disease gene for cardiomyopathies (see below). Despite the fact that the family is too small for traditional genome-wide linkage analysis to identify the genetic cause of the disease (the logarithm of the odds score of 2.1, ie, odds ratio 1:125, is well below the threshold of 3.0, ie, odds ratio 1:1000), interrogation of the entire genome adds substantial weight to a likely causative role of the titin missense mutation for disease: no other plausible mutations, including larger genomic reorganizations (copy number variants), were detected in any other genes in the linkage regions, and the remainder of the genome is excluded by negative logarithm of the odds scores.

Titin has been implicated in cardiac and skeletal muscle disease, occasionally involving a combination of both. Mutations in this gene have been described in various forms of cardiomyopathy, such as DCM, arrhythmogenic right ventricular cardiomyopathy, hypertrophic cardiomyopathy, and restrictive cardiomyopathy (reviewed in Chauveau et al[27]). Truncating variants in titin (TTNtv) are the most

frequent genetic finding in idiopathic DCM, being present in 15% to 25% of the cases,[32] and are also frequent in peripartum cardiomyopathy (15%).[33] However, penetrance seems to be low because TTNtv are also found in ≈1% of normal populations, and hence, the large majority of carriers do not manifest with disease.[34] More recent work[35] showed that DCM causing TTNtv are enriched in the sarcomeric A-band region, whereas TTNtv found in control cohorts tend to spare the A-band region and are in exons, with low usage in cardiac transcripts. An internal promotor in titin rescuing TTNtv N-terminally of the A-band region may explain this phenomenon.[36]

Titin missense mutations have been identified in DCM and hypertrophic cardiomyopathy cohorts.[4,37,38] A causative role for *TTN* p. W976R in DCM is well supported by cosegregation within a large family and functional data.[39,40] However, generally, titin missense mutations are challenging to interpret because rare benign variants are common in normal population cohorts. In the ExAC database, more than a third of the individuals carry a rare missense variant in titin (21 939 missense variants with <0.01% allelic frequency in 58 687 exomes), and although a proportion of these may represent recessive pathogenic alleles,[27] only a small fraction will be disease-causing with dominant inheritance. Hence, clinical practitioners require cosegregation information to assign causality because bioinformatic prediction tools can only give probabilistic data.[4,37] As we document here, interrogation of the entire genome combined with linkage analysis can help to narrow down lists of potential causative variants, even in small families.

Our finding of *TTN* p.A178D in a family with features of LVNC expands the spectrum of titinopathies: to our knowledge, this is the first report of a titin missense mutation implicated in cardiomyopathy with predominant features of LVNC and one of the first titin missense mutations supported by robust genome-wide genetics and detailed functional data. The latter suggests a likely pathogenic role of titin A178D by (1) evidence of protein degradation, partial unfolding, and domain destabilization in vitro, (2) protein destabilization in 2 cellular systems, and (3) altered binding properties to the ligand telethonin. Although extrapolations from such in vitro experiments on isolated domains to the full-length giant protein are not without uncertainty, such parameters will be useful complements in the future studies of other *TTN* missense variants. It is currently unclear how this particular mutation leads to this distinct phenotype, and more insight into the biology of Z-disk titin is needed to understand the underlying disease pathways. This will be addressed with the help of model organisms[36,41] or patient-derived induced pluripotent stem cell–derived cardiomyocytes,[40] focussing on the titin–telethonin complex[29] and its downstream signaling targets[42] in future work.

Acknowledgments

We thank Stephan Lange (UCSD) for a titin Z1Z2 expression construct. Small-angle x ray scattering (SAXS) data were collected at the beamline P12, operated by EMBL, Hamburg unit, at the PETRA III storage ring (DESY, Hamburg, Germany). We gratefully thank Dmitry Svergun and his group for help with the SAXS data, the SPC facility at EMBL Hamburg for technical support, and Annabel Parret for her help with the Tridetector Analysis.

Sources of Funding

Dr Gehmlich is supported by British Heart Foundation Grants (FS/12/40/29712, PG/15/113/31944). Drs Gehmlich, Hastings, and Watkins acknowledge support from the BHF Centre of Research Excellence, Oxford (grant codes HSRNWBY, HSRNWB11, and RE/13/1/30181). K.L. Thomson is the recipient of a National Institute for Health Research (NIHR) doctoral fellowship (NIHR-HCS-D13-04-006). This publication includes independent research supported also by the NIHR Biomedical Research Centre, Oxford. The work was supported also by funding from the Wellcome Trust Core Award Grant Number 090532/Z/09/Z. The views expressed are those of the authors and not necessarily those of the Department of Health or Wellcome Trust. Dr Gautel and A. Ghisleni were supported by the EU MUZIC network, the MRC, and the Leducq Foundation. Dr Gautel holds the BHF Chair of Molecular Cardiology.

Disclosures

None.

Appendix

From the Division of Cardiovascular Medicine in the Radcliffe Department of Medicine, University of Oxford, and BHF Centre of Research Excellence, United Kingdom (R.H., C.P.d.V., C.H., L.O., K.L.T., L.A., H.W., K.G.); NIHR Biomedical Research Centre Oxford (A.P., S.J.L.K., J.C.T.) and Wellcome Trust Centre for Human Genetics (A.P., S.L., S.S., S.J.L.K., J.C.T.), University of Oxford, United Kingdom; Department of Clinical Genetics, Churchill Hospital, Oxford University NHS Trust, Oxford, United Kingdom (K.L.T., E.B.); European Molecular Biology Laboratory, Hamburg, Germany (S.D.C., P.V.K., M.W.); Laboratory of Reflectometry and Small-Angle Scattering, A.V. Shubnikov Institute of Crystallography, Russian Academy of Sciences, Moscow, Russian Federation (P.V.K.); and Randall Division of Cell and Molecular Biophysics and Cardiovascular Division, King's College London BHF Centre of Research Excellence, London, United Kingdom (E.E., A.G., M.G.).

References

1. Watkins H, Ashrafian H, Redwood C. Inherited cardiomyopathies. *N Engl J Med*. 2011;364:1643–1656. doi: 10.1056/NEJMra0902923.
2. Jarcho JA, McKenna W, Pare JA, Solomon SD, Holcombe RF, Dickie S, et al. Mapping a gene for familial hypertrophic cardiomyopathy to chromosome 14q1. *N Engl J Med*. 1989;321:1372–1378. doi: 10.1056/NEJM198911163212005.
3. 1000 Genomes Project Consortium; Abecasis GR, Auton A, Brooks LD, DePristo MA, Durbin RM, et al. An integrated map of genetic variation from 1,092 human genomes. *Nature*. 2012;491:56–65. doi: 10.1038/nature11632.
4. Haas J, Frese KS, Peil B, Kloos W, Keller A, Nietsch R, et al. Atlas of the clinical genetics of human dilated cardiomyopathy. *Eur Heart J*. 2015;36:1123–1135a. doi: 10.1093/eurheartj/ehu301.
5. Watkins H. Assigning a causal role to genetic variants in hypertrophic cardiomyopathy. *Circ Cardiovasc Genet*. 2013;6:2–4. doi: 10.1161/CIRCGENETICS.111.000032.
6. Jenni R, Oechslin E, Schneider J, Attenhofer Jost C, Kaufmann PA. Echocardiographic and pathoanatomical characteristics of isolated left ventricular non-compaction: a step towards classification as a distinct cardiomyopathy. *Heart*. 2001;86:666–671.
7. Petersen SE, Selvanayagam JB, Wiesmann F, Robson MD, Francis JM, Anderson RH, et al. Left ventricular non-compaction: insights from cardiovascular magnetic resonance imaging. *J Am Coll Cardiol*. 2005;46:101–105. doi: 10.1016/j.jacc.2005.03.045.
8. Purcell S, Neale B, Todd-Brown K, Thomas L, Ferreira MA, Bender D, et al. PLINK: a tool set for whole-genome association and population-based linkage analyses. *Am J Hum Genet*. 2007;81:559–575. doi: 10.1086/519795.
9. Abecasis GR, Cherny SS, Cookson WO, Cardon LR. Merlin–rapid analysis of dense genetic maps using sparse gene flow trees. *Nat Genet*. 2002;30:97–101. doi: 10.1038/ng786.
10. Taylor JC, Martin HC, Lise S, Broxholme J, Cazier JB, Rimmer A, et al. Factors influencing success of clinical genome sequencing across a broad spectrum of disorders. *Nat Genet*. 2015;47:717–726. doi: 10.1038/ng.3304.
11. Lunter G, Goodson M. Stampy: a statistical algorithm for sensitive and fast mapping of Illumina sequence reads. *Genome Res*. 2011;21:936–939. doi: 10.1101/gr.111120.110.

12. Rimmer A, Phan H, Mathieson I, Iqbal Z, Twigg SR, Wilkie AO, et al.; WGS500 Consortium. Integrating mapping-, assembly- and haplotype-based approaches for calling variants in clinical sequencing applications. *Nat Genet*. 2014;46:912–918. doi: 10.1038/ng.3036.
13. McLaren W, Pritchard B, Rios D, Chen Y, Flicek P, Cunningham F. Deriving the consequences of genomic variants with the Ensembl API and SNP Effect Predictor. *Bioinformatics*. 2010;26:2069–2070. doi: 10.1093/bioinformatics/btq330.
14. Landrum MJ, Lee JM, Riley GR, Jang W, Rubinstein WS, Church DM, et al. ClinVar: public archive of relationships among sequence variation and human phenotype. *Nucleic Acids Res*. 2014;42(Database issue):D980–D985. doi: 10.1093/nar/gkt1113.
15. Zou P, Gautel M, Geerlof A, Wilmanns M, Koch MH, Svergun DI. Solution scattering suggests cross-linking function of telethonin in the complex with titin. *J Biol Chem*. 2003;278:2636–2644. doi: 10.1074/jbc.M210217200.
16. Geier C, Gehmlich K, Ehler E, Hassfeld S, Perrot A, Hayess K, et al. Beyond the sarcomere: CSRP3 mutations cause hypertrophic cardiomyopathy. *Hum Mol Genet*. 2008;17:2753–2765. doi: 10.1093/hmg/ddn160.
17. Reinhard L, Mayerhofer H, Geerlof A, Mueller-Dieckmann J, Weiss MS. Optimization of protein buffer cocktails using Thermofluor. *Acta Crystallogr Sect F Struct Biol Cryst Commun*. 2013;69(pt 2):209–214. doi: 10.1107/S1744309112051858.
18. Shaya D, Kreir M, Robbins RA, Wong S, Hammon J, Brüggemann A, et al. Voltage-gated sodium channel (NaV) protein dissection creates a set of functional pore-only proteins. *Proc Natl Acad Sci U S A*. 2011;108:12313–12318. doi: 10.1073/pnas.1106811108.
19. Fürst DO, Osborn M, Nave R, Weber K. The organization of titin filaments in the half-sarcomere revealed by monoclonal antibodies in immunoelectron microscopy: a map of ten nonrepetitive epitopes starting at the Z line extends close to the M line. *J Cell Biol*. 1988;106:1563–1572.
20. Gehmlich K, Asimaki A, Cahill TJ, Ehler E, Syrris P, Zachara E, et al. Novel missense mutations in exon 15 of desmoglein-2: role of the intracellular cadherin segment in arrhythmogenic right ventricular cardiomyopathy? *Heart Rhythm*. 2010;7:1446–1453. doi: 10.1016/j.hrthm.2010.08.007.
21. Cameron JM, Maj M, Levandovskiy V, Barnett CP, Blaser S, Mackay N, et al. Pyruvate dehydrogenase phosphatase 1 (PDP1) null mutation produces a lethal infantile phenotype. *Hum Genet*. 2009;125:319–326. doi: 10.1007/s00439-009-0629-6.
22. Carrilho-Ferreira P, Almeida AG, Pinto FJ. Non-compaction cardiomyopathy: prevalence, prognosis, pathoetiology, genetics, and risk of cardioembolism. *Curr Heart Fail Rep*. 2014;11:393–403. doi: 10.1007/s11897-014-0227-3.
23. Walsh R, Thomson KL, Ware JS, Funke BH, Woodley J, McGuire KJ, et al. Reassessment of mendelian gene pathogenicity using 7,855 cardiomyopathy cases and 60,706 reference samples. *Genet Med*. 2016. doi: 10.1038/gim.2016.90.
24. Labeit S, Kolmerer B, Linke WA. The giant protein titin. Emerging roles in physiology and pathophysiology. *Circ Res*. 1997;80:290–294.
25. Wang K, McClure J, Tu A. Titin: major myofibrillar components of striated muscle. *Proc Natl Acad Sci U S A*. 1979;76:3698–3702.
26. Gerull B. The rapidly evolving role of titin in cardiac physiology and cardiomyopathy. *Can J Cardiol*. 2015;31:1351–1359. doi: 10.1016/j.cjca.2015.08.016.
27. Chauveau C, Rowell J, Ferreiro A. A rising titan: TTN review and mutation update. *Hum Mutat*. 2014;35:1046–1059. doi: 10.1002/humu.22611.
28. Hidalgo C, Granzier H. Tuning the molecular giant titin through phosphorylation: role in health and disease. *Trends Cardiovasc Med*. 2013;23:165–171. doi: 10.1016/j.tcm.2012.10.005.
29. Bertz M, Wilmanns M, Rief M. The titin-telethonin complex is a directed, superstable molecular bond in the muscle Z-disk. *Proc Natl Acad Sci U S A*. 2009;106:13307–133310. doi: 10.1073/pnas.0902312106.
30. Zou P, Pinotsis N, Lange S, Song YH, Popov A, Mavridis I, et al. Palindromic assembly of the giant muscle protein titin in the sarcomeric Z-disk. *Nature*. 2006;439:229–233. doi: 10.1038/nature04343.
31. Truong K, Ikura M. The use of FRET imaging microscopy to detect protein-protein interactions and protein conformational changes in vivo. *Curr Opin Struct Biol*. 2001;11:573–578.
32. Herman DS, Lam L, Taylor MR, Wang L, Teekakirikul P, Christodoulou D, et al. Truncations of titin causing dilated cardiomyopathy. *N Engl J Med*. 2012;366:619–628. doi: 10.1056/NEJMoa1110186.
33. Ware JS, Li J, Mazaika E, Yasso CM, DeSouza T, Cappola TP, et al.; IMAC-2 and IPAC Investigators. Shared genetic predisposition in peripartum and dilated cardiomyopathies. *N Engl J Med*. 2016;374:233–241. doi: 10.1056/NEJMoa1505517.
34. Watkins H. Tackling the achilles' heel of genetic testing. *Sci Transl Med*. 2015;7:270fs1. doi: 10.1126/scitranslmed.aaa4276.
35. Roberts AM, Ware JS, Herman DS, Schafer S, Baksi J, Bick AG, et al. Integrated allelic, transcriptional, and phenomic dissection of the cardiac effects of titin truncations in health and disease. *Sci Transl Med*. 2015;7:270ra6. doi: 10.1126/scitranslmed.3010134.
36. Zou J, Tran D, Baalbaki M, Tang LF, Poon A, Pelonero A, et al. An internal promoter underlies the difference in disease severity between N- and C-terminal truncation mutations of Titin in zebrafish. *Elife*. 2015;4:e09406. doi: 10.7554/eLife.09406.
37. Begay RL, Graw S, Sinagra G, Merlo M, Slavov D, Gowan K, et al; Familial Cardiomyopathy Registry. Role of titin missense variants in dilated cardiomyopathy. *J Am Heart Assoc*. 2015;4:. doi: 10.1161/JAHA.115.002645.
38. Lopes LR, Zekavati A, Syrris P, Hubank M, Giambartolomei C, Dalageorgou C, et al.; Uk10k Consortium. Genetic complexity in hypertrophic cardiomyopathy revealed by high-throughput sequencing. *J Med Genet*. 2013;50:228–239. doi: 10.1136/jmedgenet-2012-101270.
39. Gerull B, Gramlich M, Atherton J, McNabb M, Trombitás K, Sasse-Klaassen S, et al. Mutations of TTN, encoding the giant muscle filament titin, cause familial dilated cardiomyopathy. *Nat Genet*. 2002;30:201–204. doi: 10.1038/ng815.
40. Hinson JT, Chopra A, Nafissi N, Polacheck WJ, Benson CC, Swist S, et al. HEART DISEASE. Titin mutations in iPS cells define sarcomere insufficiency as a cause of dilated cardiomyopathy. *Science*. 2015;349:982–986. doi: 10.1126/science.aaa5458.
41. Gramlich M, Pane LS, Zhou Q, Chen Z, Murgia M, Schötterl S, et al. Antisense-mediated exon skipping: a therapeutic strategy for titin-based dilated cardiomyopathy. *EMBO Mol Med*. 2015;7:562–576. doi: 10.15252/emmm.201505047.
42. Knöll R, Linke WA, Zou P, Miocic S, Kostin S, Buyandelger B, et al. Telethonin deficiency is associated with maladaptation to biomechanical stress in the mammalian heart. *Circ Res*. 2011;109:758–769. doi: 10.1161/CIRCRESAHA.111.245787.

CLINICAL PERSPECTIVE

High throughput next-generation sequencing techniques have made whole genome sequencing accessible and are increasingly applied in clinical practice. However, the abundance of variation in the human genomes makes the identification of a disease-causing mutation on a background of benign rare variants challenging. To illustrate, more than one third of individuals in normal population cohorts carry a rare missense variant in the giant protein titin (coded by the gene *TTN*), but only a small fraction of these will be disease-causing with dominant inheritance. Hence, titin missense variants are currently often ignored or left uninterpreted when found in cardiomyopathy patients. Here we combine whole genome sequencing with linkage analysis in a 3-generation family affected by cardiomyopathy with features of autosomal dominant left ventricular noncompaction cardiomyopathy. A missense mutation in titin (*TTN* p. A178D) is the only plausible disease-causing variant that segregates with disease among affected individuals of the family, with interrogation of the entire genome excluding other potential causes. Functional studies on this missense mutation demonstrate domain misfolding and destabilization, resulting in paired binding to the ligand telethonin/t-cap and, hence, supporting its highly likely causative role. Our report expands the spectrum of titin's roles in cardiomyopathies and furthermore highlights that rare titin missense variants should be considered to be relevant for cardiomyopathies and can be identified by combining whole genome sequencing with linkage analysis in medium-sized cardiomyopathy families.

Circulation
Cardiovascular Genetics

Combination of Whole Genome Sequencing, Linkage, and Functional Studies Implicates a Missense Mutation in Titin as a Cause of Autosomal Dominant Cardiomyopathy With Features of Left Ventricular Noncompaction

Robert Hastings, Carin P. de Villiers, Charlotte Hooper, Liz Ormondroyd, Alistair Pagnamenta, Stefano Lise, Silvia Salatino, Samantha J.L. Knight, Jenny C. Taylor, Kate L. Thomson, Linda Arnold, Spyros D. Chatziefthimiou, Petr V. Konarev, Matthias Wilmanns, Elisabeth Ehler, Andrea Ghisleni, Mathias Gautel, Edward Blair, Hugh Watkins and Katja Gehmlich

Circ Cardiovasc Genet. 2016;9:426-435; originally published online September 13, 2016;
doi: 10.1161/CIRCGENETICS.116.001431
Circulation: Cardiovascular Genetics is published by the American Heart Association, 7272 Greenville Avenue, Dallas, TX 75231

Print ISSN: 1942-325X. Online ISSN: 1942-3268

Supplemental Material

Expanded Methods

Copy Number Analyses

Copy number analyses were carried out for all family members (see Figure 1A) except II-4 and III-2 (for whom DNA was unavailable). For each individual, ~200ng DNA was tested against a sub-array of an Illumina HumanCytoSNP-12v1 BeadChip (Illumina Inc, San Diego, CA) according to manufacturer's guidelines. Data analyses were performed with GenomeStudio v2009.2 (Illumina Inc., San Diego, CA) and finalreport.txt files uploaded into Nexus Copy Number v7.5.3 Discovery Edition (BioDiscovery, Hawthorne, CA) for visualisation and evaluation of copy number (CN) events, looking for events that that might segregate with and contribute to affected cardiomyopathy status as given in the pedigree (Figure 1A). In addition, WGS data (.bam files) from the two first cousins (III-1 and III-4) were processed using ngbin (https://github.com/) set with a window size of 1000 and read count filter of 10. The ngbin output was uploaded into Nexus Copy Number v7.5.3 Discovery Edition for visualisation and CN events evaluated and noted. In the WGS data, centromeric and telomeric peaks and peaks mapping to SD sequences were excluded. CN events were not considered relevant with respect to the cardiomyopathy phenotype if they had been noted previously at >1% frequency in unrelated datasets (Database of Genomic Variants http://dgv.tcag.ca/dgv/app/home or 'in house') or did not co-segregate in family members with a confirmed cardiomyopathy (see Figure 1).

LOD score calculation

A standard disease model for rare dominant conditions was used to calculate the LOD score: allele frequency = 0.0001 (0.01%) and probability of being affected for individuals with 0, 1 and 2 copies of the disease allele (penetrance) was 0.0001, 1.0 and 1.0 respectively (i.e. complete penetrance for heterozygotes) on Merlin (version 1.1.2) software.

Expression profiles of genes

Evidence of expression of the genes in the heart both at RNA and protein level was interrogated in following databases:

GeneCards	http://www.genecards.org/
Expression Atlas (EMBL-EBI)	https://www.ebi.ac.uk/gxa/home
The Human Protein Atlas	http://www.proteinatlas.org/
ProteomicsDB	https://www.proteomicsdb.org/
PaxDB	http://pax-db.org/#!home
GTex Portal	http://www.gtexportal.org/home/
GeneHub	http://share.gene.com/Research/genentech/genehub-gepis/index.html

Biophysical characterisation of titin Z1Z2 protein fragments

Size Exclusion Chromatography-Tridetector Analysis: The two proteins, WT Z1Z2 and the A178D mutant were analysed with a Viscotek 305 tridetector (Malvern Instruments, Malvern, UK), equipped with light scattering, refractive index, and UV absorbance detectors. Malvern was connected to an analytical size exclusion column (Superdex 200 10/300 GL; GE Healthcare), at a flow rate of 0.3 mL/min, using 25 mm Tris (pH 8.0), 200 mm NaCl as running buffer. The protein

concentration was 3.6 and 3.8 mg/mL for the WT and A178D respectively and the sample volume was 100 µl. The refractive index combined with light-scattering data were used for the estimation of the molecular masses. BSA, re-suspended in the same buffer, was used as internal control.

Circular Dichroism (CD) spectropolarimetry measurements: Prior to each measurement, the two samples were dialyzed against 10 mM potassium phosphate, pH 7.5, 100 mM NaF and diluted to 10 µM. The spectra were recorded on a Chirascan CD Spectrometer (Applied Photophysics), between 190 and 260 nm, at 10°C, using a 0.5 mm cuvette. The background was subtracted and each spectrum was converted to mean residue ellipticity. Each curve represents the average of three measurements.

Thermal stability assay: The thermal stability of the two variants was assessed by differential scanning fluorimetry (Thermofluor™), using a iCycleMyIQ RT-PCR Detection System (Bio-Rad), equipped with a CCD detector for imaging of the fluorescence. SYPRO Orange was added as a fluorophore. The protein was concentrated at 50 and 100 µM, in a buffer containing 25 mm Tris (pH 8.0) and 200 mm NaCl. The plate was heated from 5 to 95 °C with initial stepwise increments of 1 °C per minute. Each curve represents the average of five separate measurements.

SAXS measurements and data processing: Synchrotron radiation X-ray scattering data were collected on the EMBL P12 beamline at the PETRA III storage ring (DESY, Hamburg). Solutions of Z1Z2 WT and A178D mutant were measured at 10 °C at solute concentrations of 2.7, 5,6 and 10.3 mg/ml. PILATUS 2M detector (Dectris, Switzerland) was used at the sample-detector distance 3.0 m and wavelength λ=0.1 nm, covering the momentum transfer range $0.05 < s < 4.5$ nm^{-1} (s

= $4\pi \sin\theta/\lambda$, where 2θ is the scattering angle). The samples had no measurable radiation damage detected by comparison of twenty successive time frames with 50 ms exposures. The data were averaged after normalization to the intensity of the transmitted beam and the scattering of the buffer was subtracted. The difference data were extrapolated to zero solute concentration following standard procedures. All data manipulations were performed using the program package PRIMUS [1].

The radius of gyration R_g of solutes and the forward scattering $I(0)$ were evaluated using the Guinier approximation at small angles ($s < 1.3/R_g$) [2] (assuming that the intensity is represented as $I(s) = I(0)\ exp(-(sR_g)^2/3)$ and also from the entire scattering pattern by the program GNOM [3]. In the latter case the distance distribution functions $p(r)$ and the maximum particle dimensions D_{max} were also computed. The molecular masses (MM) of the solutes were evaluated by comparison of the calculated $I(0)$ value with that of the standard solution of bovine serum albumin (MM 66 kDa).

The excluded volumes of hydrated protein molecules (V_p) were calculated using the Porod approximation:

$$V_p = 2\pi^2 I(0) / \int_0^\infty s^2 I_{exp}(s) ds \qquad (1)$$

in which the intensity $I(s)$ was modified by subtraction of an appropriate constant from each data point to force the s^{-4} decay of the intensity at higher angles following the Porod's law [4] for homogeneous particles.

Low resolution *ab initio* model of Z1Z2 WT and A178D mutant were generated by the program DAMMIF [5], which represents the protein by an assembly of densely packed beads. Simulated annealing (SA) was employed to build a compact

interconnected configuration of beads that fits the experimental data $I_{exp}(s)$ to minimize the discrepancy:

$$\chi^2 = \frac{1}{N-1}\sum_j \left[\frac{I(s_j) - cI_{calc}(s_j)}{\sigma(s_j)}\right]^2 \qquad (2)$$

where N is the number of experimental points, c is a scaling factor, $I_{calc}(s_j)$ and $\sigma(s_j)$ are the calculated intensity and the experimental error at the momentum transfer s_j, respectively. The common structural features of the model were determined by superimposing and averaging of the configurations from ten separate runs using the programs SUPCOMB [6] and DAMAVER [7].

The scattering pattern of the crystallographic coordinates of wild-type Z1Z2 (PDB code: 2A38) was calculated using CRYSOL [8]. Given the atomic coordinates, the program fits the experimental intensity by adjusting the excluded volume of the particle and the contrast of the hydration layer to minimize the discrepancy, defined by χ^2 (equation 2).

Foerster Resonance Energy Transfer Experiments

WT human titin Z1Zr3 was cloned in the expression vector pECFP-C1 between the XhoI and BamHI restriction sites, with an N-terminal CFP-tag. The same plasmid was used for site-directed mutagenesis of the titin Z1Zr3 A178D construct. Wild-type human telethoninΔC (residues 1-90) was cloned in the expression vector pEYFP-C1 between the XhoI and BamHI restriction sites, with N-terminal YFP-tag. Sequences were validated by DNA sequencing.

COS-1 cells were cultured in Dulbecco's modified Eagle medium supplemented with 10% fetal bovine serum and 100 U/mL penicillin/streptomycin (Invitrogen Life Technologies). For expression and microscopic analysis of

fluorescent fusion proteins, cells were grown on plastic slides and transfected with appropriate plasmid DNA using Escort IV transfection reagent (Sigma-Aldrich, USA) according to the manufacturer's instructions. Cells were fixed for 10 min with 4% paraformaldehyde 24–36 h post-transfection and specimens were mounted in anti-fade medium.

To detect FRET by the acceptor photobleaching method, cells transfected with appropriate combinations of donor and acceptor expression constructs were imaged on a Zeiss LSM 510 confocal microscope using a 63X 1.4NA Plan NeoFluar oil immersion objective. CFP was excited with the 458 nm line of an Argon-Krypton ion laser and YFP was excited using the 514 nm argon line, respectively. A 545 nm dichroic mirror was used to split the two emission channels, followed by a band-pass 475–525 nm filter for the CFP channel and a long pass 530 nm filter for the YFP channel. The coverslip was first scanned at 10x magnification, marking cells showing strong comparable signals for both CFP and YFP channels. During preliminary scans with the 63X Objective, a rectangular acquisition Region of Interest (ROI) was chosen where homogeneous signals for each channel were detected. The gain for the CFP and YFP channels were set to the nearest grey-value to maximum without saturating any pixels, at approximately 75% of the dynamic range (12-bit, 4096 grey levels), with offsets set such that backgrounds were zero. Any saturated pixels were automatically excluded from FRET calculations in order to not affect FRET results. Time-lapse mode was used to collect one pre-bleach image for each channel before bleaching. YFP was photobleached using the 514 nm line at maximum power for 150 iterations. A second post-bleach image was then collected for each channel. Pre and post-bleach CFP and YFP images were processed using the software Image-J (NIH) and user-written Macros. Images were background-subtracted using rolling ball

radius (sliding paraboloid, 3.0-5.0 pixels radius), and pre- and post-bleach images fade-corrected. FRET efficiency (E_r) was calculated according to equation (3):

$$E_r = (CFP_{postbleach} - CFP_{prebleach}) / CFP_{postbleach} \quad (3)$$

By using the equation (4):

$$E_{ext} = E_r / Bleach_{efficiency} \quad (4)$$

FRET efficiency can be extrapolated to theoretical bleach efficiency 100% (E_{ext}) according to the linear correlation previously described [9]. Mean values from three independent cell transfections were plotted for comparison. Error bars represent standard deviations. Unpaired student's test was performed and $p < 0.05$ was considered significant.

Assessment of protein stability

Human Titin Z1Z2 WT and A178D were cloned into the pShuttle-hrGFP-2 vector (Agilent). Adenoviral particles were generated, scaled up and purified using the AdEasy system (Agilent) according to the manufacturer's instructions. NRC were infected at MOI = 5 and harvested after 48 hrs. Total protein extracts were generated and assayed by Western blotting as described [10] using anti-HA monoclonal rat antibody (Roche), anti-hrGFP polyclonal rabbit antibody (Agilent) and anti-GAPDH polyclonal rabbit antibody (Millipore). Western blots were quantified using ImageLab software (Biorad), intensity normalised to loading control and expressed relative to Z1Z2 WT (set to 100 %). RNA was isolated from identically infected NRC using the RNeasy Mini kit (Qiagen) and transcribed with High Capacity cDNA Reverse transcription Kit (Applied Biosystems) prior to amplification reactions performed using Fast Universal Master Mix on a StepOnePlus system (Applied Biosystems). Samples were run in duplicate in a total reaction volume of 10 µL. Following TaqMan

assays were used: human recombinant titin (not detecting rat *Ttn*): Hs01562028_m1, rat *Gapdh*: Rn99999916_s1 (both inventoried), hrGFP – assay ID AIY9YGZ (custom designed). Relative expression was quantified using the comparative CT method.

COS-1 cells were cultured and transfected as for the FRET experiments using HA-tagged constructs coding for human titin Z1Z2 WT or A178D (1 mug DNA for WT and 2.5 mug for A178D, respectively). Cells were treated with translational inhibitor cycloheximide at 20 mug/ml for 8 and 24 hrs, vehicle control (DMSO) was applied for 24 hrs. Total protein extracts were prepared and blotted for HA-tag as above and beta-actin as loading control (polyclonal rabbit antibody, Sigma). Western blots were quantified using ImageLab software (Biorad), intensity normalised to loading control and expressed relative to vehicle control values (set to 100 %).

Additional Figures

Figure S1: Cardiac MRI images demonstrating prominent features of LVNC in affected individuals III-3, III-4 and III-5, but not III-6. II-4 has a dilated LV. End-diastolic four chamber views are shown, numbering of individuals as in Figure 1A and Table 1.

Figure S2: Linkage plots for each chromosome from SNP array data analysed in MERLIN software. Red lines indicate a LOD score of 0 and the approximate positions of *TTN* and *PDP2* are indicated by arrows.

Figure S3: A – Comparison of DNA sequence between a synthetically derived reference sequence (top panel) and individual II-4 (middle panel). The heterozygous missense variant is indicated by the black arrow. The bottom panel illustrates the signal-to-noise ratio between the reference sequence and the patient sequence. The presence of the heterozygous single nucleotide variant *TTN* c.533C>A (*TTN* p. A178D) is clearly distinguishable (raised peak) from the background noise (using Mutation Surveyor software, Softgenetics).

B – Structural alignment using deposited structures of titin Ig-domains. The position of beta-strands A to G is marked and the position of A178 indicated with an asterisk. Apart from Alanine, position 178 is exclusively occupied by hydrophobic side chains (Val, Leu, Ile) or cysteine. Structural alignment was performed by PDBeFold (SSM) [11] using secondary structure matching. Sequence conservation analysis was done by the ConSruf server [12].

Figure S4 – Thermal denaturation experiments: Titin Z1Z2 WT (solid line) unfolds with a melting temperature of approximately 62 degrees. Titin Z1Z2 A178D (broken line) displays high fluorescence signal already at low temperatures, and no melting temperature can be deducted for Titin Z1Z2 A178D.

Figure S5 SAXS measurements: A – Normalized Kratky plot displays a bell-shaped profile for Z1Z2 WT (1, black symbols) typical for folded structures, whereas for the A178D mutant (2, white symbols) it appears to be intermediate between folded and completely unfolded structures [13] suggesting the presence of unfolded parts/flexible domains in the A178D mutant. B – Scattering patterns from Z1Z2 WT (1) and Z1Z2 A178D (2) and their models: experimental data (WT in black and A178D in white dots) are shown with error bars representing one standard deviation; scattering computed from *ab initio* models are plotted with solid lines, scattering from the monomeric Z1Z2 WT model (PDB code: 2A38) with dashed lines. Insert: Distance distribution functions *p(r)* for Z1Z2 WT (black symbols) and for Z1Z2 A178D (white symbols). The asymmetric tails of the distance distribution functions for both Z1Z2 WT and Z1Z2 A178D are consistent with an elongated shape of the proteins.

Figure S6 A – Control experiments to demonstrate equal MOIs for WT and A178D in experiments shown in Figure 4B. Quantification of Western blots from Figure 4C is shown in grey bars. For mRNA measurements (black bars), NRCs were transfected as in Figure 4C and analysed RNA quantified by TaqMan assays for human titin Z1Z2 and the hrGFP reporter. B, C – Pulse chase experiments confirming reduced stability of titin Z1Z2 A178D protein fragment in COS-1 cells. B – Cells were transfected with constructs coding for HA-tagged titin Z1Z2 WT (left) or titin Z1Z2

A178D (right) mutant protein fragment and treated with cycloheximide (CHX) to stop protein translation for 8 and 24 hours. Vehicle treated cells (24 hrs) served as control. Expression of HA-tagged titin Z1Z2 was assayed from total protein lysates by Western blotting for HA-tag, probing for endogenous beta-actin served as loading control. C – Quantification of HA-tagged titin Z1Z2 normalised to beta-actin: Amounts are shown relative to vehicle control (set to 100 %). Titin Z1Z2 WT fragment (grey bars) is more stable than titin Z1Z2 A178D mutant protein fragment (black bars).

Figure S7. NRC were transfected with titin Z1Z2 WT or A178D as in Figure 4D, but counterstained for endogenous telethonin. Merged images are shown in the third row, HA shown in red, endogenous telethonin in green. No changes in localisation are observed for telethonin in the presence of titin Z1Z2 A178D. Scale bar represents 10 microns.

Additional Tables

Table S1: Filtering criteria applied to all variants identified.

Table S2: Variants remaining after automated filtering.

Table S3: Analysis and exclusion of an intronic/ splice region variant in titin.

Table S4: Primer sequences.

Supplemental References

1. Konarev PV, Volkov VV, Sokolova AV, Koch MHJ, Svergun DI. PRIMUS: a Windows PC-based system for small-angle scattering data analysis. *J Appl Crystallogr*. 2003;36:1277-1282.

2. Guinier A. La diffraction des rayons X aux tres petits angles; application a l'etude de phenomenes ultramicroscopiques. *Ann Phys (Paris)* 1939;12:161-237.

3. Svergun D. Determination of the regularization parameter in indirect-transform methods using perceptual criteria. *J Appl Crystallogr.* 1992;25:495-503.

4. Porod G. General theory. In: O. K. Glatter, O., ed. *Small-angle X-ray scattering* London: Academic Press; 1982.

5. Franke D, Svergun DI. DAMMIF, a program for rapid ab-initio shape determination in small-angle scattering. *J Appl Crystallogr.* 2009;42:342-346.

6. Kozin MB, Svergun DI. Automated matching of high- and low-resolution structural models. *J Appl Crystallogr.* 2001;34:33-41.

7. Volkov VV, Svergun DI. Uniqueness of ab initio shape determination in small-angle scattering. *J Appl Crystallogr.* 2003;36:860-864.

8. Svergun D, Barberato C, Koch MHJ. CRYSOL - a Program to Evaluate X-ray Solution Scattering of Biological Macromolecules from Atomic Coordinates. *J Appl Crystallogr.* 1995;28:768-773.

9. Menon RP, Soong D, de Chiara C, Holt MR, Anilkumar N, Pastore A. The importance of serine 776 in Ataxin-1 partner selection: a FRET analysis. *Sci Rep.* 2012;2:919.

10. Geier C, Gehmlich K, Ehler E, Hassfeld S, Perrot A, Hayess K , et al. Beyond the sarcomere: CSRP3 mutations cause hypertrophic cardiomyopathy. *Hum Mol Genet*. 2008;17:2753-2765.

11. Krissinel E, Henrick K. Inference of macromolecular assemblies from crystalline state. *J Mol Biol*. 2007;372:774-797.

12. Celniker G, Nimrod G, Ashkenazy H, Glaser F, Martz E, Mayrose I , et al. ConSurf: Using Evolutionary Data to Raise Testable Hypotheses about Protein Function. *Isr J Chem*. 2013;53:199-206.

13. Receveur-Brechot V, Durand D. How random are intrinsically disordered proteins? A small angle scattering perspective. *Curr Protein Pept Sci*. 2012;13:55-75.

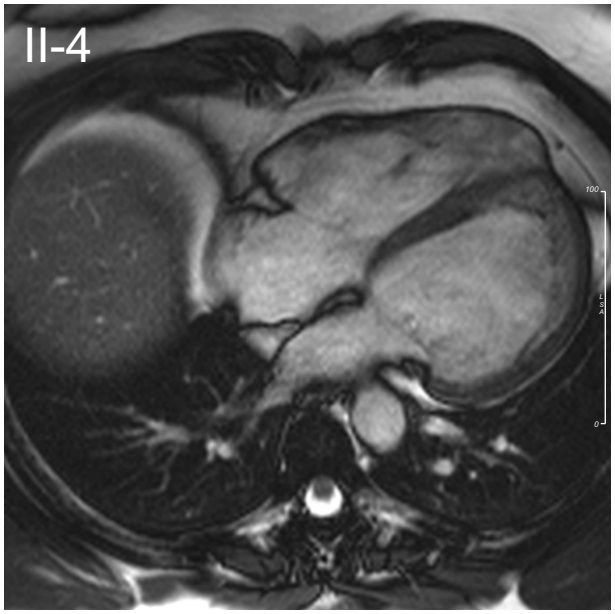

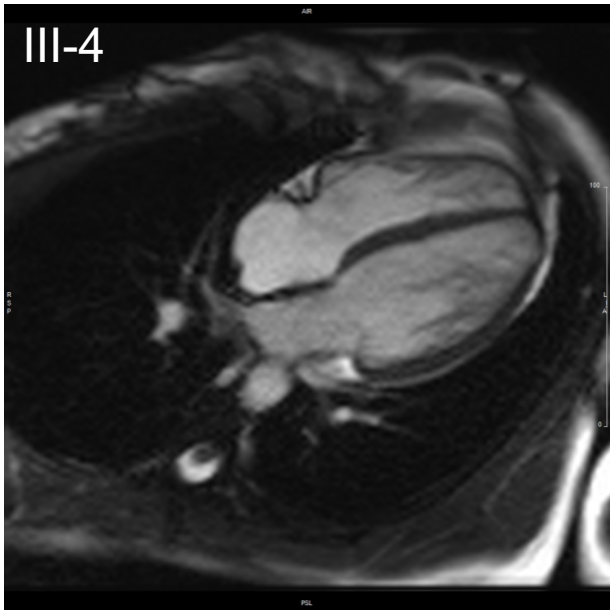

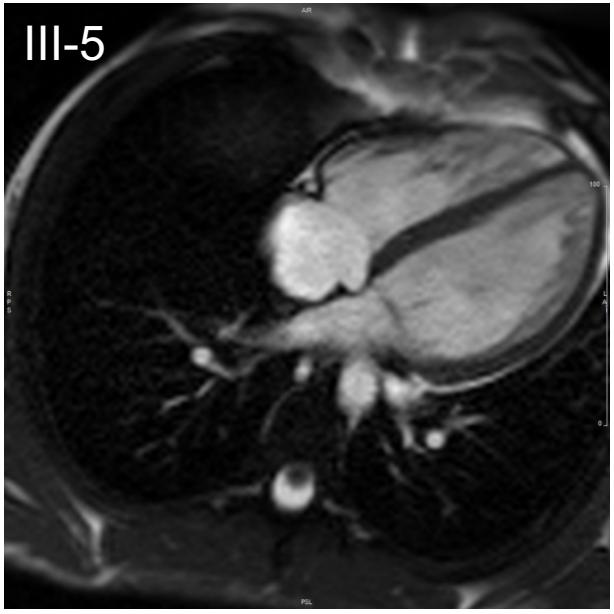

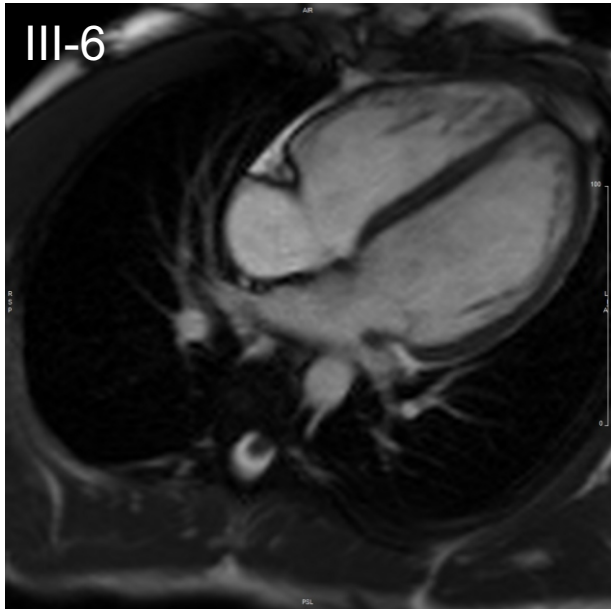

Figure S1

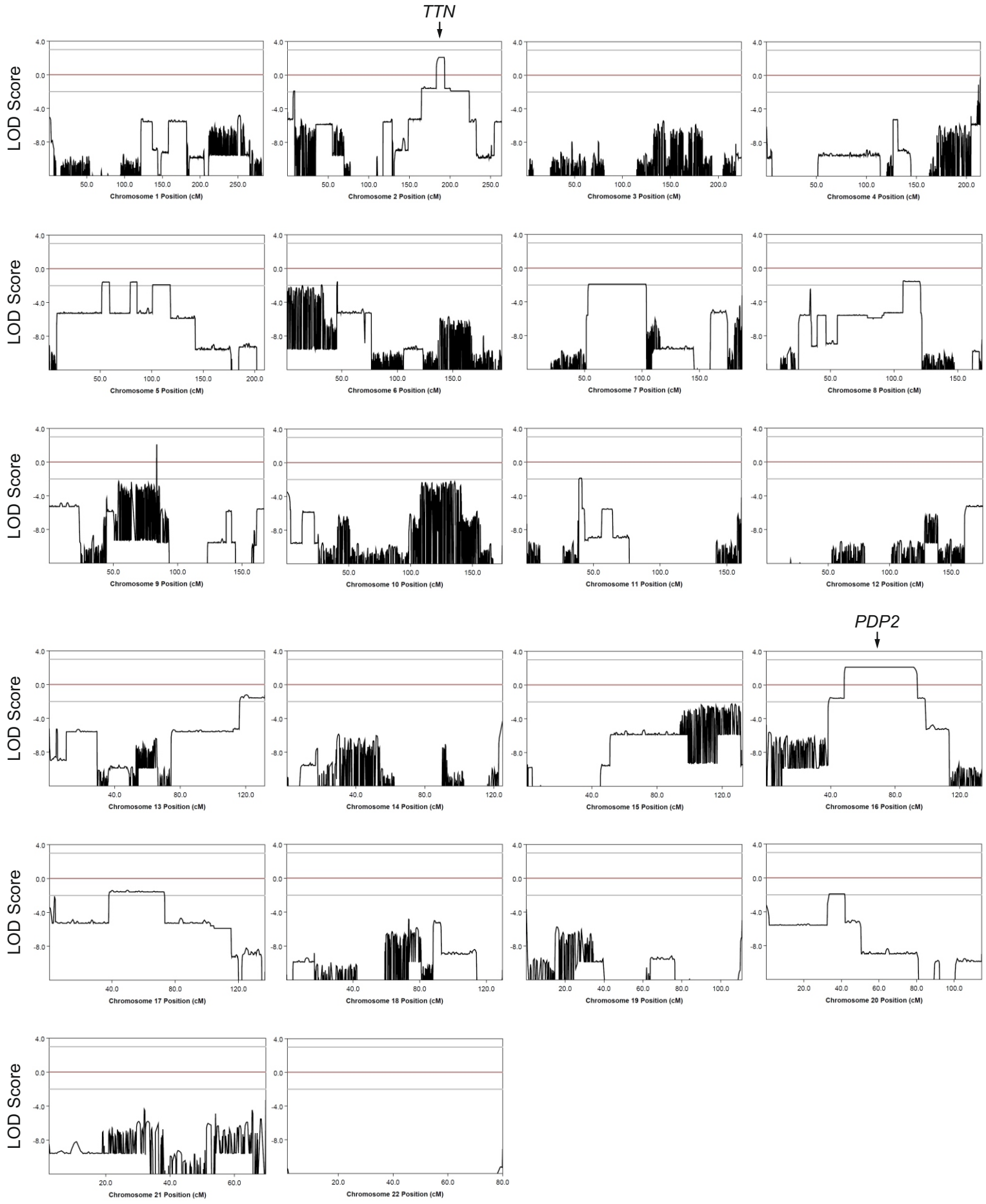
TTN
PDP2
LOD Score
4.0
0.0
-4.0
-8.0
Chromosome 1 Position (cM)
Chromosome 2 Position (cM)
Chromosome 3 Position (cM)
Chromosome 4 Position (cM)
Chromosome 5 Position (cM)
Chromosome 6 Position (cM)
Chromosome 7 Position (cM)
Chromosome 8 Position (cM)
Chromosome 9 Position (cM)
Chromosome 10 Position (cM)
Chromosome 11 Position (cM)
Chromosome 12 Position (cM)
Chromosome 13 Position (cM)
Chromosome 14 Position (cM)
Chromosome 15 Position (cM)
Chromosome 16 Position (cM)
Chromosome 17 Position (cM)
Chromosome 18 Position (cM)
Chromosome 19 Position (cM)
Chromosome 20 Position (cM)
Chromosome 21 Position (cM)
Chromosome 22 Position (cM)

Figure S2

A

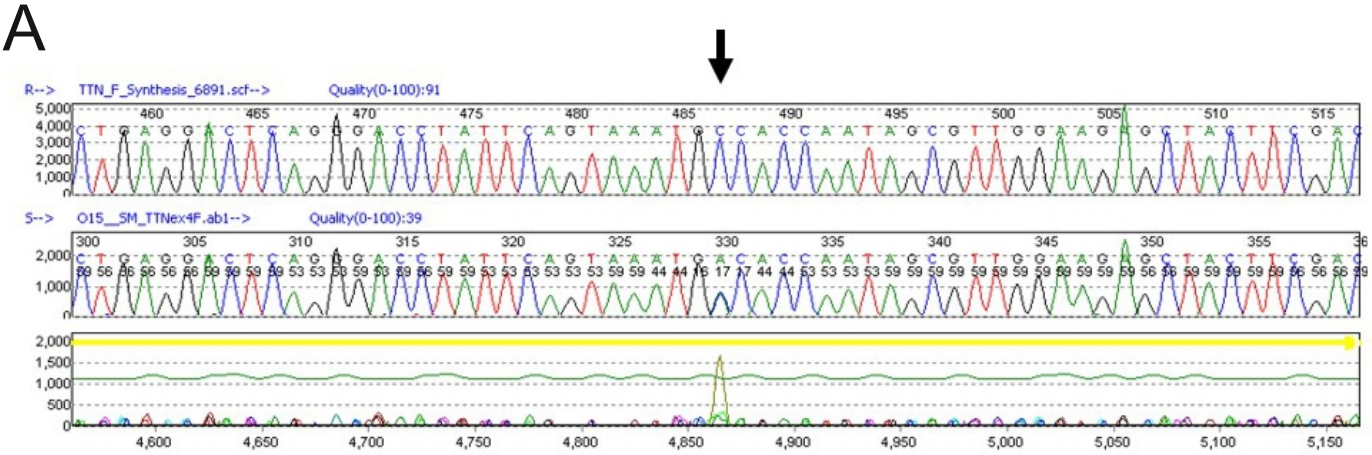
R--> TTN_F_Synthesis_6891.scf--> Quality(0-100):91
S--> O15__SM_TTNex4F.ab1--> Quality(0-100):39

B

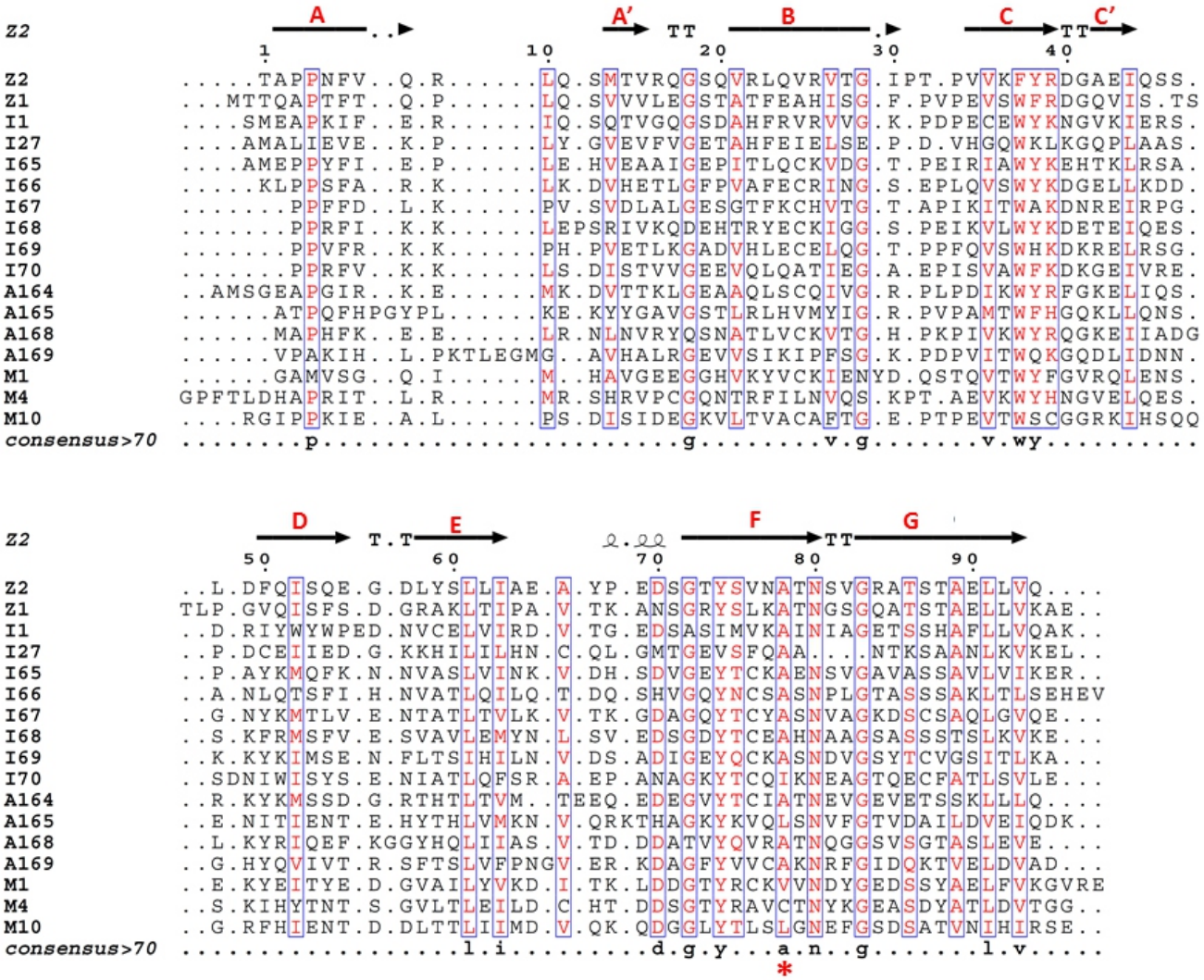
Z2
A
A'
B
C
C'
D
E
F
G
Z2
Z1
I1
I27
I65
I66
I67
I68
I69
I70
A164
A165
A168
A169
M1
M4
M10
consensus>70

Figure S3

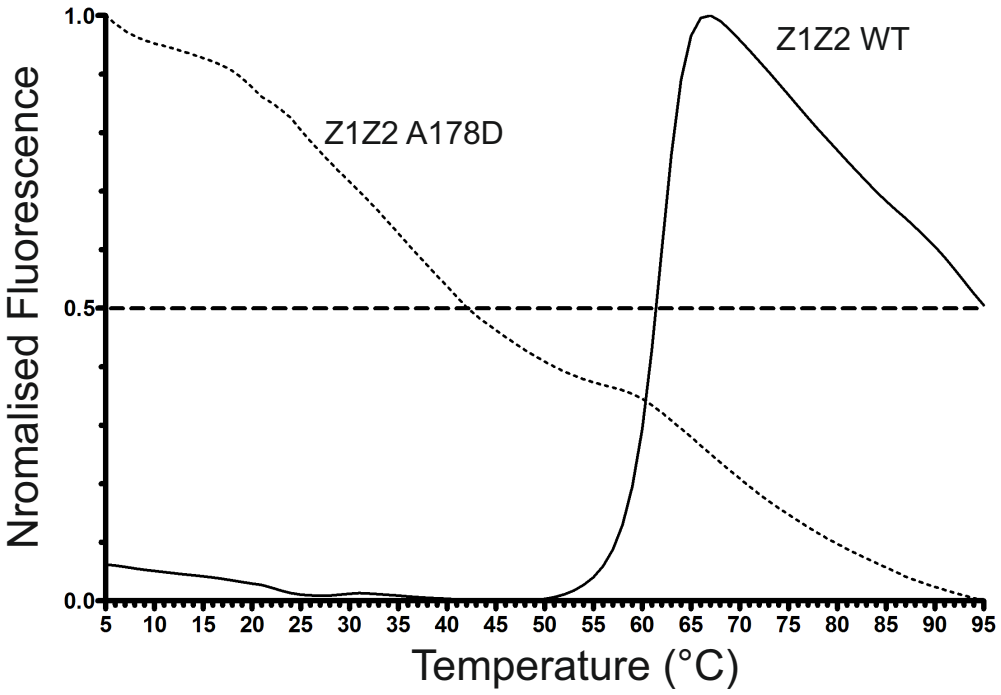
Nromalised Fluorescence
1.0
0.5
0.0
5 10 15 20 25 30 35 40 45 50 55 60 65 70 75 80 85 90 95
Temperature (°C)
Z1Z2 WT
Z1Z2 A178D

Figure S4

A

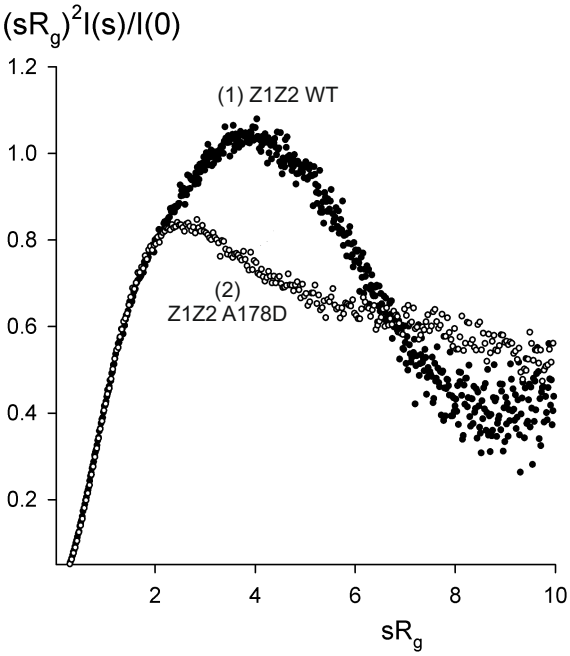
(sR$_g$)^{2}I(s)/I(0)
1.2
1.0
0.8
0.6
0.4
0.2
(1) Z1Z2 WT
(2)
Z1Z2 A178D
2
4
6
8
10
sR$_g$

B

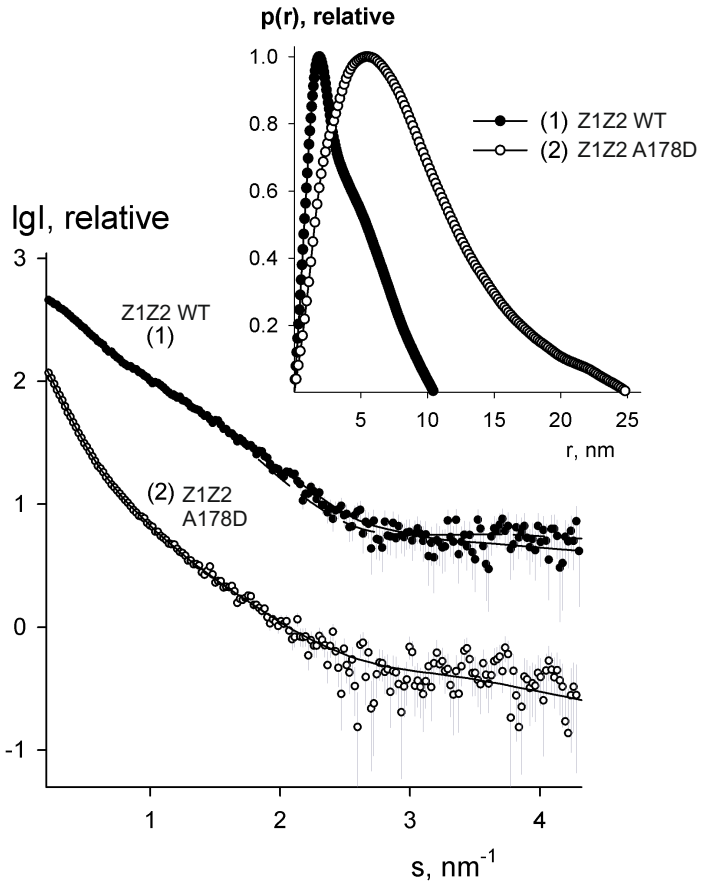
p(r), relative
1.0
0.8
0.6
0.4
0.2
(1) Z1Z2 WT
(2) Z1Z2 A178D
5
10
15
20
25
r, nm
lgI, relative
3
2
1
0
-1
Z1Z2 WT
(1)
(2) Z1Z2
A178D
1
2
3
4
s, nm^{-1}

Figure S5

A

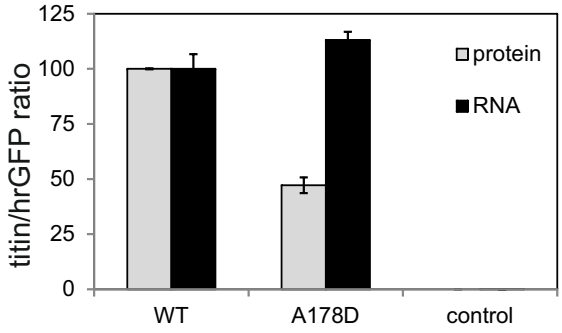

B

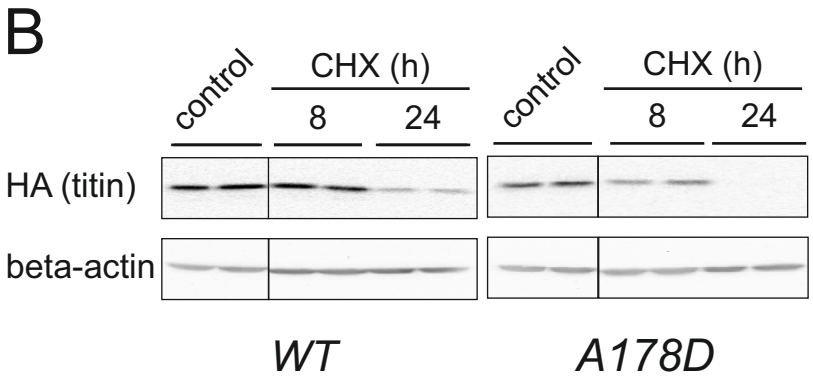

C

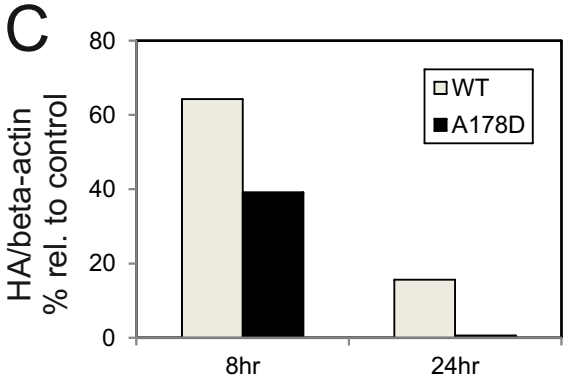

Figure S6

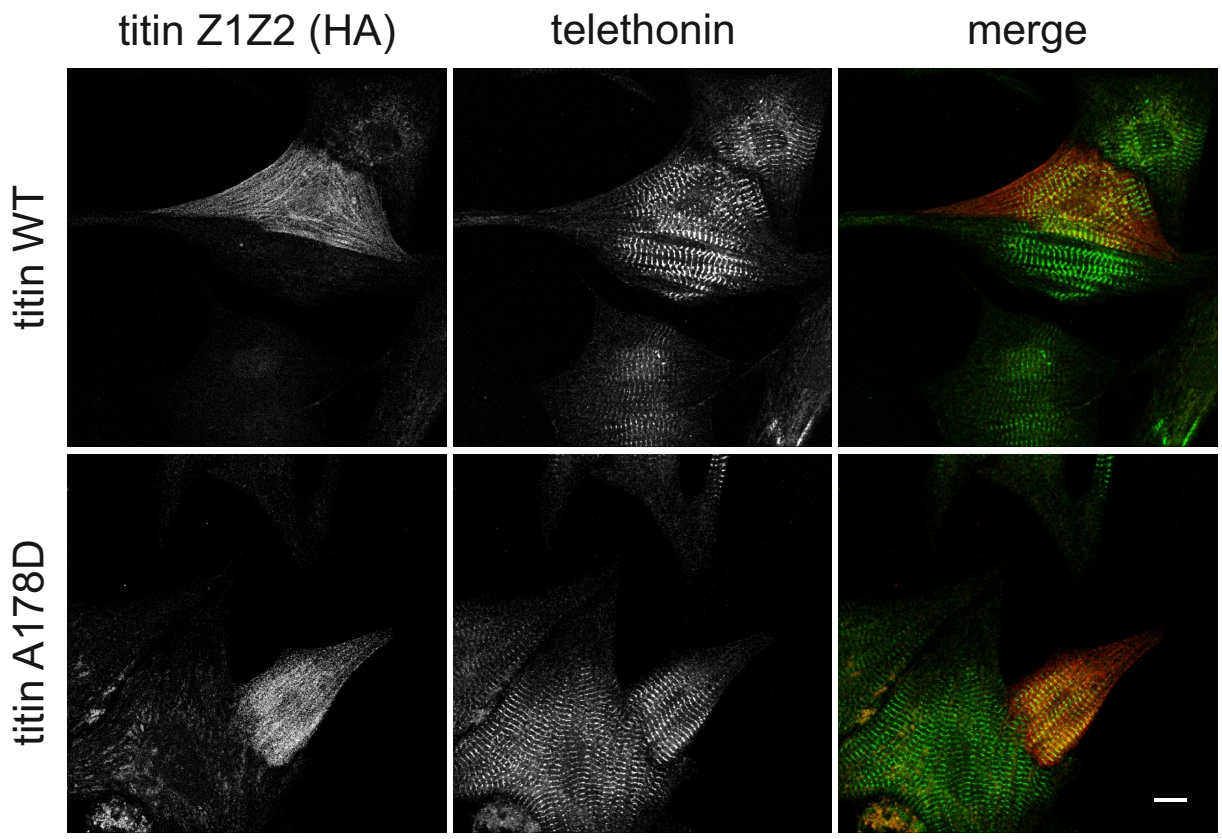

Figure S7

Table S1: Filtering criteria applied to all variants identified.

1. Within linkage region (LOD > 0), whereby both affected and unaffected individuals were considered in the linkage analysis

2. Exonic or splicing variant,
   i.e. with one of the following consequence terms: 'transcript_ablation', 'splice_donor_variant', 'splice_acceptor_variant', 'stop_gained', 'frameshift_variant', 'stop_lost', 'initiator_codon_variant', 'transcript_amplification', 'inframe_insertion', 'inframe_deletion', 'missense_variant', 'splice_region_variant'

3. Heterozygous and shared by both affected individuals (III-1 and III-4)

4. Called confidently by Platypus (flagged as 'PASS')

5. Overlapping neither segmental duplications nor repeats

6. Allele frequency in 1000 Genomes ≤ 1 % or not reported [1]

7. Observed no more than 7 times in WGS500 [2]

8. Observed no more than 50 times in ESP
   (Exome Variant Server, http://evs.gs.washington.edu/EVS/)

9. Observed no more than 50 times in UK10K
   (UK10K Project, http://www.uk10k.org)

10. Observed no more than 500 times in ExAC Browser
    (Exome Aggregation Consortium, http://exac.broadinstitute.org/)

Steps 1 to 10 are implemented in an automated script, further filtering steps are based on manual inspection:

11. Supporting evidence for the existence of affected transcript(s)

12. Evidence of expression of the gene in the heart both at RNA and protein level using multiple databases (see Expanded Materials)

13. Splice/intronic variants: considered if at crucial position (-2 to +2) or violating consensus rules at position -6 to -3 (for 5' sites) or at position -3 for 3' sites [3]

    Predicted to be tolerated using MaxEntScan
    (http://genes.mit.edu/burgelab/maxent/Xmaxentscan_scoreseq.html and
    http://genes.mit.edu/burgelab/maxent/Xmaxentscan_scoreseq_acc.html)

References Table S1

1. 1000 Genomes Project Consortium, Abecasis GR, Auton A, Brooks LD, DePristo MA, Durbin RM , et al. An integrated map of genetic variation from 1,092 human genomes. *Nature*. 2012;491:56-65.

2. Taylor JC, Martin HC, Lise S, Broxholme J, Cazier JB, Rimmer A , et al. Factors influencing success of clinical genome sequencing across a broad spectrum of disorders. *Nat Genet*. 2015;47:717-726.

3. Padgett RA. New connections between splicing and human disease. *Trends Genet*. 2012;28:147-154.

Table S2: Variants remaining after Platypus filtering (steps 1-10 of Table S1)

											Allele frequency				
CHROMOSOME	**POSITION**	**REFERENCE**	**ALTERATION**	**QUALITY**	**FILTER**	**GENE**	**CONSEQUENCE**	**AA_CHANGE**	**SIFT**	**POLYPHEN**	**1000G**	**UK10K(AC/AN)**	**ESP6500(AC/AN)**	**EXAC**	**Reason for exclusion**
16	66919133	G	A	1484	PASS	*PDP2*	missense_variant	E316K	deleterious(0)	probably_damaging(1)	0	1.3E-04	0	4.9E-05	n/a
2	179665172	G	T	1658	PASS	*TTN*	missense_variant	A178D	deleterious(0)	possibly damaging (0.734)	0	0	0	0	n/a
16	31495991	C	T	1852	PASS	*SLC5A2*	splice_region_variant & intron_variant				0	0	0	8.2E-06	expressed exclusively in kidney and testis; position -3 of a 3' splice junction, predicted to be tolerated
16	67208979	G	T	1242	PASS	*NOL3*	missense_variant	G45V		unknown(0)	0	0	0	2.5E-05	an artefact due to an incorrect, poorly supported transcript (ENST00000564860) present in Ensembl; synonymous R213R change in all other transcripts
2	176995495	C	T	1044	PASS	*HOXD8*	missense_variant	A134V	tolerated(0.08)	benign(0.31)	0	0	0	0	not present in affected individual III-6
2	179414205	A	G	1005	PASS	*TTN*	splice_region_variant & intron_variant				0	0	0	0	position -5 of a 3' splice junction, predicted to be tolerated (for detailed analysis see Table S3)

RNA and protein expression in the heart

GENE	**RNA**					**Protein**					**Comment**
	GeneCards	Expression Atlas (EMBL)	Protein Atlas	GeneHub	GTex	Protein Atlas	Human Protein Map	Proteomics DB	PaxDB	GeneCards	
TTN	✓	✓	✓	✓	✓	✓	✓	✓	✓	✓	*known cardiomyopathy gene*
PDP2	✓	✓	✓	✗	✓ (low)	✓	✗	✗	✗	✗	*low expression in the heart*

Table S3: Analysis and exclusion of an intronic/splice region variant in titin.

Position 2:179,414,205	**Reference**	**Variant**
base	A	G

Position	- 5 position of 3' splice intron /exon 339 boundary (ENST00000589042)
Affected exon [1]	Fibronectin domain in A-band titin Percentage spliced in (PSI) of exon 339: 100 (DCM), 98 (controls)

Percentage Spliced In (PSI) Prediction		**Reference**
SPANR	difference in PSI score between refence and variant: 0.8 %	http://tools.genes.toronto.edu/

Conservation PhyloP poor

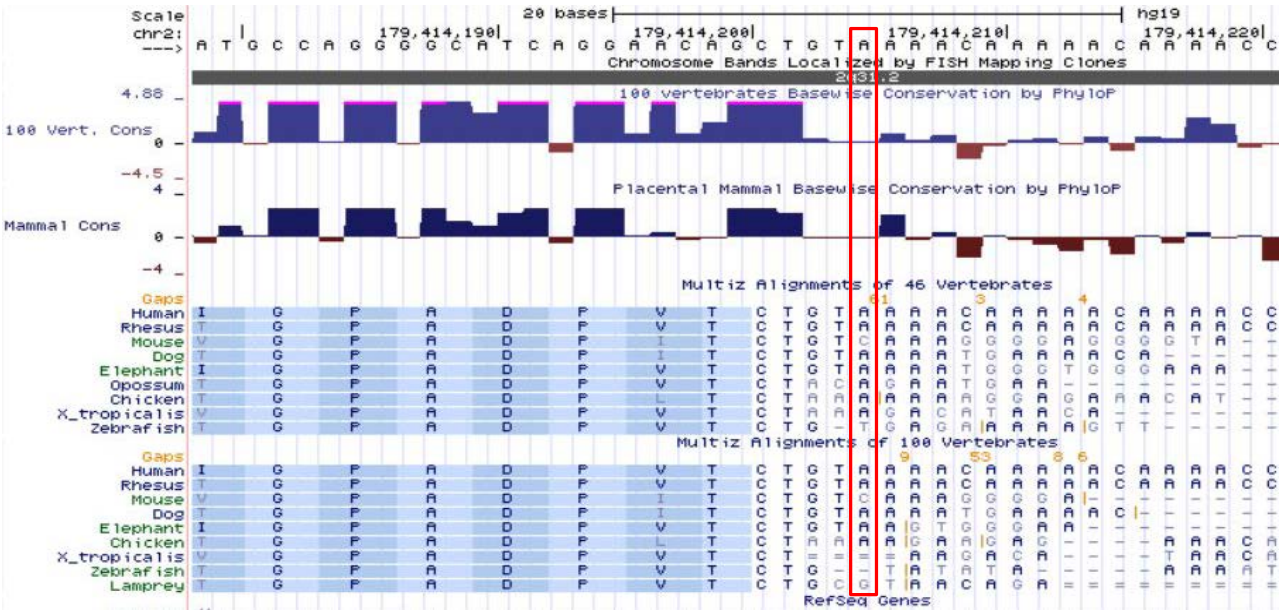

Splice Prediction

Tool	**Reference**	**Variant**	**Difference**	**Percent**	**Consequence**	**Reference**
MaxEntScan	11.08	9.94	1.14	10%	tolerated (< 15 %, [2])	http://genes.mit.edu/burgelab/maxent/Xmaxentscan_scoreseq_acc.html
VEP-MaxEntScan	11.08	10.90	0.15	1.4%	tolerated (< 15 %, [2])	
BDGP	0.99	0.98	0.01	1.0%	tolerated (cut off 0.40)	www.fruitfly.org/seq_tools/splice.html
Summary Alamut Visual v2.6	Predicted change at acceptor site 5 bps downstream: -7.8%				"not predictable"	
SpliceSiteFinder	93.8	92.4	1.4	1.5%		Alamut Visual (Interactive Biosoftware)
NNSPLICE	1.0	0.9	0.1	10.0%		Alamut Visual (Interactive Biosoftware)
GeneSplicer	7.5	4.7	2.8	37.0%		Alamut Visual (Interactive Biosoftware)
Human Splicing Finder	90.5	86.9	3.6	4.0%		Alamut Visual (Interactive Biosoftware)

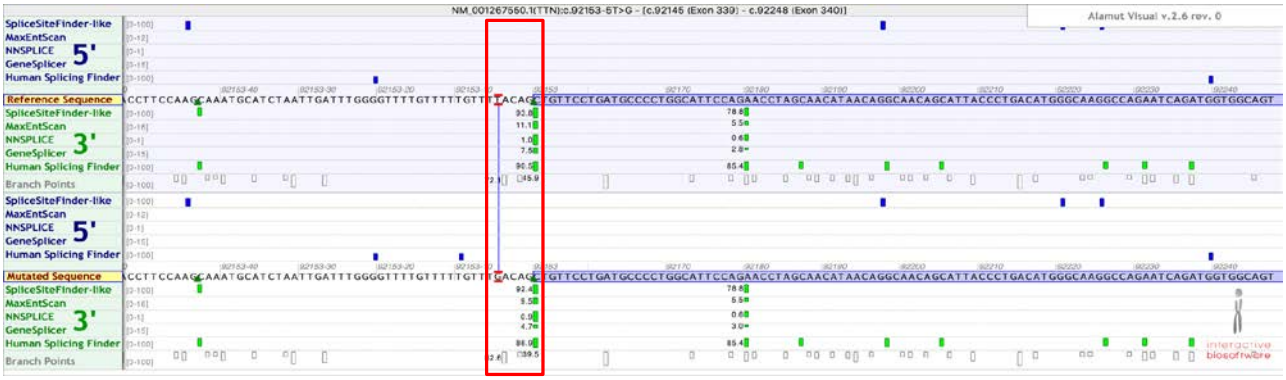

References

[1] Roberts AM, Ware JS, Herman DS, Schafer S, Baksi J, Bick AG , et al. Integrated allelic, transcriptional, and phenomic dissection of the cardiac effects of titin truncations in health and disease. *Science Translational Medicine* . 2015;7:270ra6.

[2] Houdayer C, Caux-Moncoutier V, Krieger S, Barrois M, Bonnet F, Bourdon V, et al. Guidelines for splicing analysis in molecular diagnosis derived from a set of 327 combined in silico/in vitro studies on BRCA1 and BRCA2 variants. *Hum Mutat.* 2012; 33(8):1228-38.

Table S4: Primer sequences

Sanger sequencing

TTN A178D

Forward 5’ –TCACCTGGTTTTGGAATTGG – 3’

Reverse 5’ –GGCCCCATTTAGACACAAAC – 3’

PDP2 E316K

Forward 5’ –CTGGAAGATGAGGTGACAAGG – 3’

Reverse 5’ –ATCTGAGGCCAGCACAAGG – 3’

Cloning primer (restriction sites in capital letters)

Telethonin amino acids 1-90 pEBG

Forward 5’ – tttGGATCCatggctacctcagagctgagc -3’

Reverse 5’ – tttGCGGCCGCttacggcagtacccgctggtag – 3’

Telethonin amino acids 1-167 pEBG

Forward 5’ – tttGGATCCatggctacctcagagctgagc -3’

Reverse 5’ – tttGCGGCCGCtcagcctctctgtgcttcctg -3’

Titin Z1Z2 pShuttle IRES hrGFP-2

Forward 5’- tttGCGGCCGCcccaccatgacaactcaagcaccgacg - 3’

Reverse 5’- tttCGATCGGaccttgaaccagtaattcagcag -3’

Titin Z1Z2 into pEGFP-N1

Forward 5’- tttCTCGAGatgacaactcaagcaccgacg – 3’

Reverse 5’- tttGGATCCcgaccttgaaccagtaattcagcag – 3’

Titin Z1Zr3 into pECFP-C1 (FRET)

Forward 5’ –tttctcgagccATGACAACTCAAGCACCGAC 3’

Reverse 5’ –ttggatcctcaGTAACTCAAGAAGCAATAAGA -3’

TelethoninΔC (amino acids 1-90) into pEYFP-C1 (FRET)

Forward 5’ –tttctcgagccATGGCTACCTCAGAGCTGAGC -3’

Reverse 5’ –ttggatcctcaCGGCAGTACCCGCTGGTAG – 3’

Mutagenesis *TTN* A178D

Forward 5’ – ACTCAGGGACCTATTCAGTAAATGaCACCAATAGCG – 3’

Reverse 5’ – CGCTATTGGTGtCATTTACTGAATAGGTCCCTGAGT – 3’